Towards Characterization of the First Stars and Galaxies (and Beyond) with Low-frequency Radio Observations

Piyanat (Boom) Kittiwisit

Arizona State University (ASU), University of KwaZulu-Natal (UKZN)

Collaborators

ASU (USA): Judd Bowman, Daniel Jacobs, Adam Beardsley, Steven Murray

NRAO (USA): Nithya Thyagarajan, UKZN (SA): Yin-Zhe Ma

NARIT, July 19, 2019

Cosmology (and Beyond) with Low-frequency Radio Observations

Piyanat (Boom) Kittiwisit

Arizona State University (ASU), University of KwaZulu-Natal (UKZN)

Collaborators

ASU (USA): Judd Bowman, Daniel Jacobs, Adam Beardsley, Steven Murray

NRAO (USA): Nithya Thyagarajan, UKZN (SA): Yin-Zhe Ma

NARIT, July 19, 2019

Outline

- Part I – Overview of Low-frequency Cosmology
- Part II – My Work on Statistical Analysis of Low-frequency Cosmology Data
- Part III – Beyond Cosmology – Examples of Space Weather Physics from Low-frequency Radio Observations

When and how were the first stars and galaxies formed and evolved into modern large-scale structure?

Recombination | Dark Ages | **Reionization** | Modern Galaxies

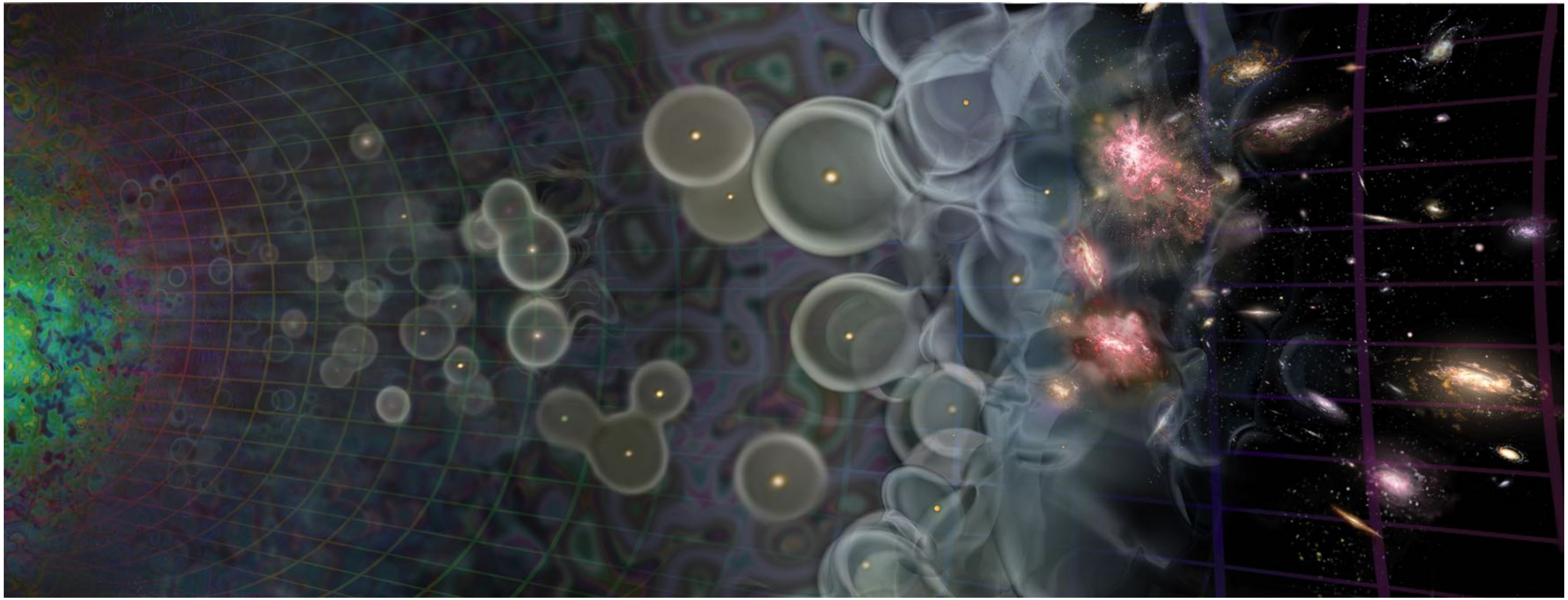

z=1100 400kyr | z=13 370Myr | z=6 1Gyr | z=0 Today 13.7Gyr

Figure: Loeb/Scientific American

21 cm lines can be used to probe reionization

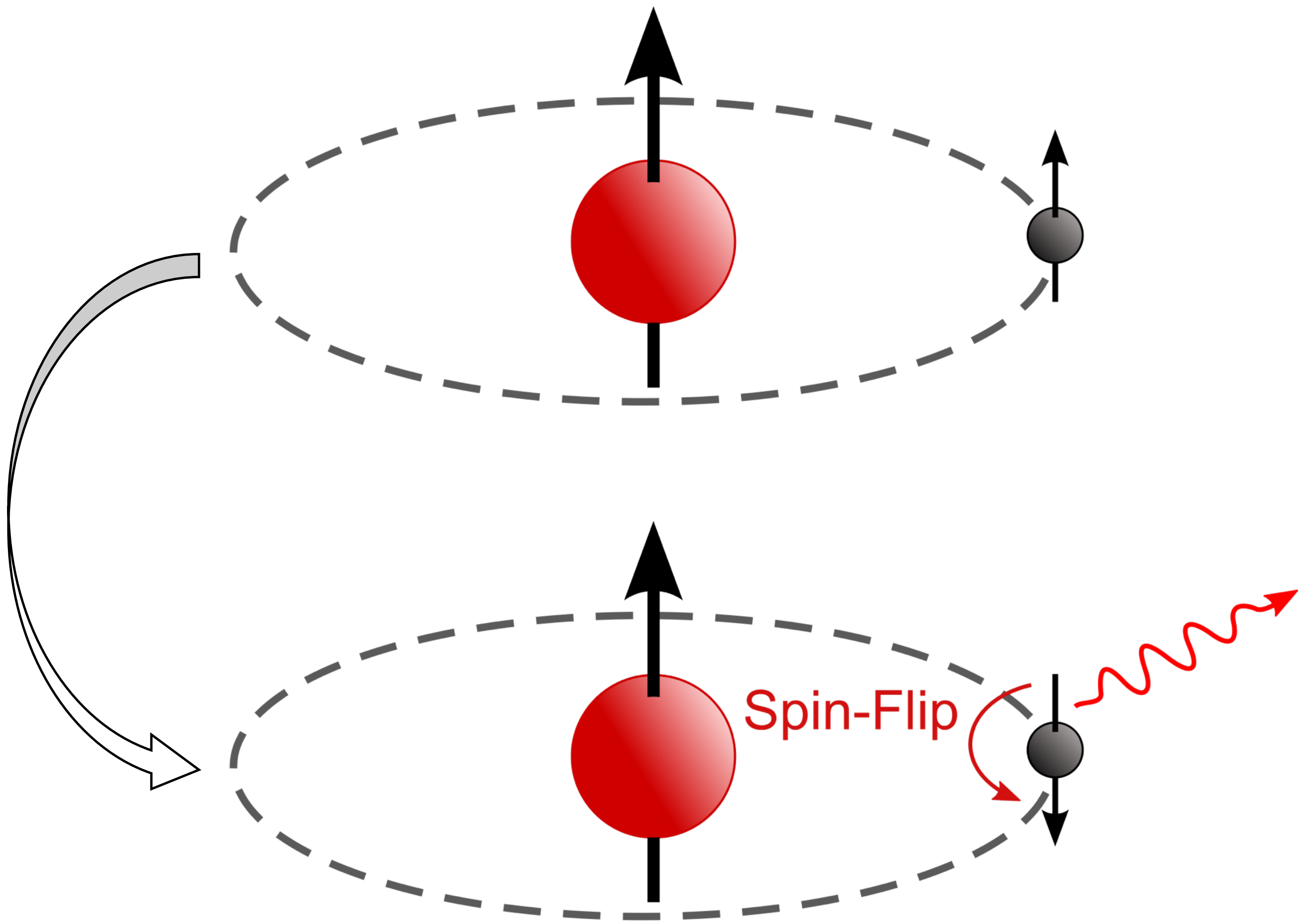

$$\lambda_0 = 21\text{cm}$$

$$\nu_0 = 1420 \text{ MHz}$$

21 cm lines can be used to probe reionization

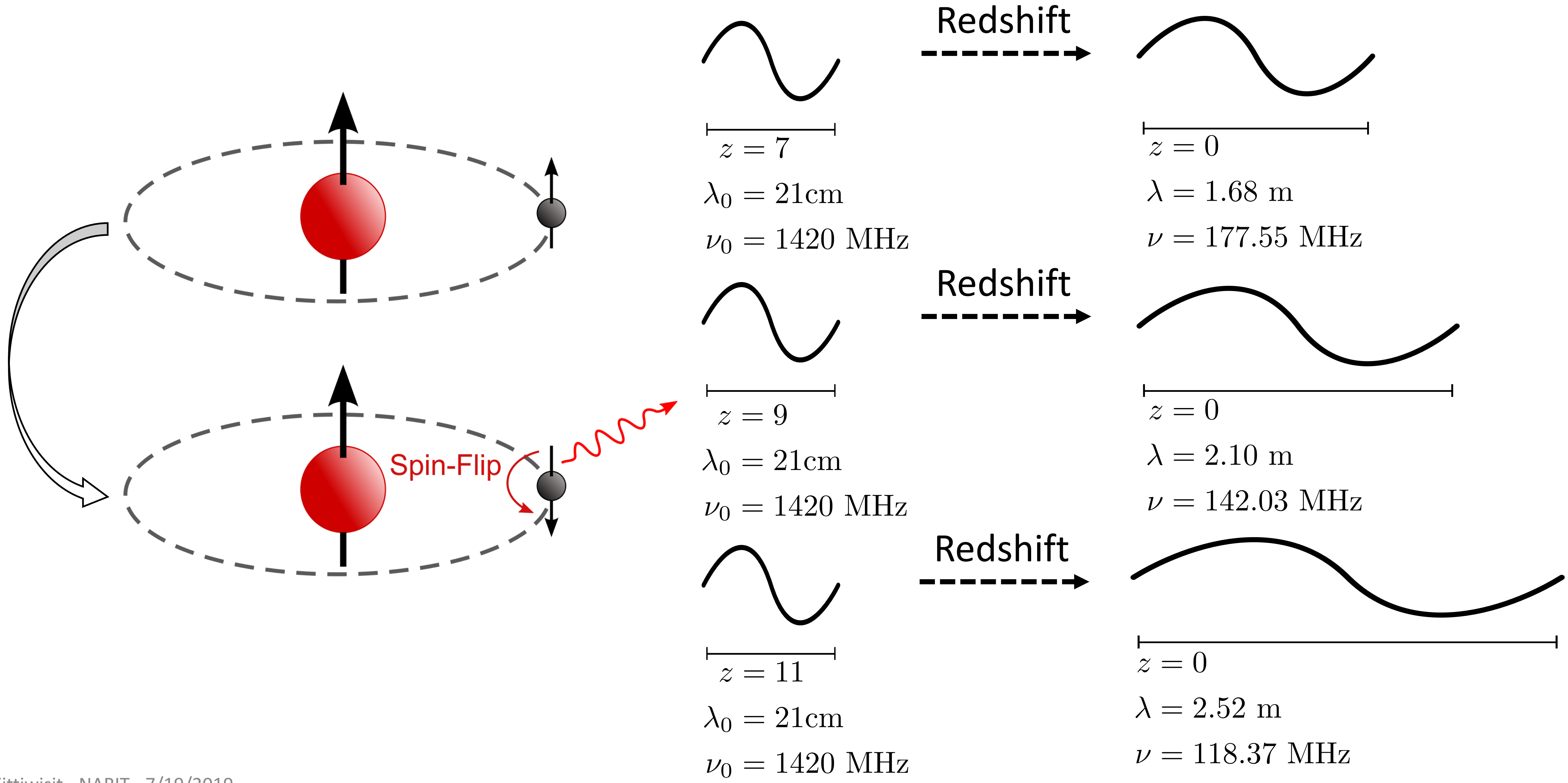

21 cm Brightness Temperature Fluctuations

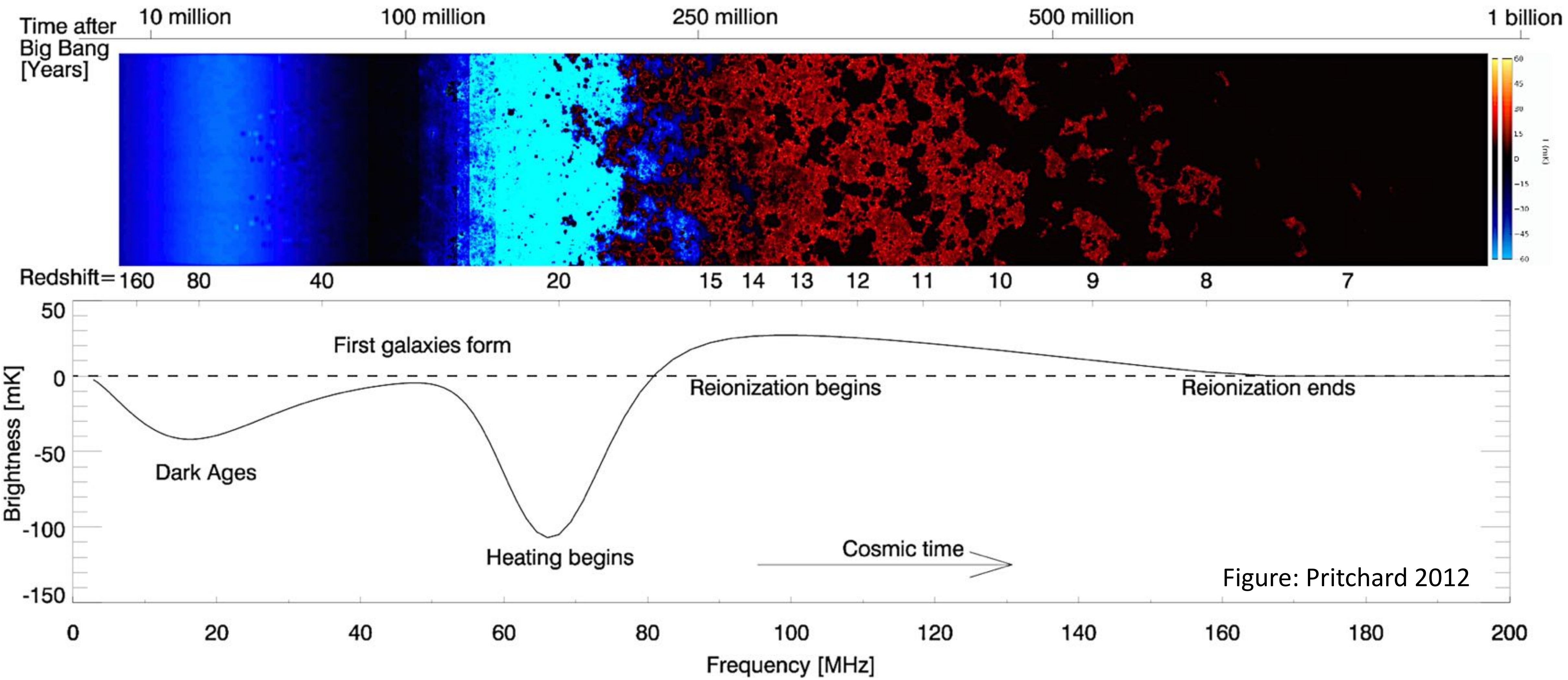

$$\delta T_b(r_\parallel) \approx 9 x_{HI}(r_\parallel)(1+\delta(r_\parallel))(1+z)^{1/2}\left[1-\frac{T_\gamma}{T_S}\right]\left[\frac{H(z)/(1+z)}{\mathrm{d}v_\parallel/\mathrm{d}r_\parallel}\right]\ \mathrm{mK}.$$

See Madau et al. 1997 for derivation

Currently Operating and Future Experiments

Challenges #1: Telescope response is complex

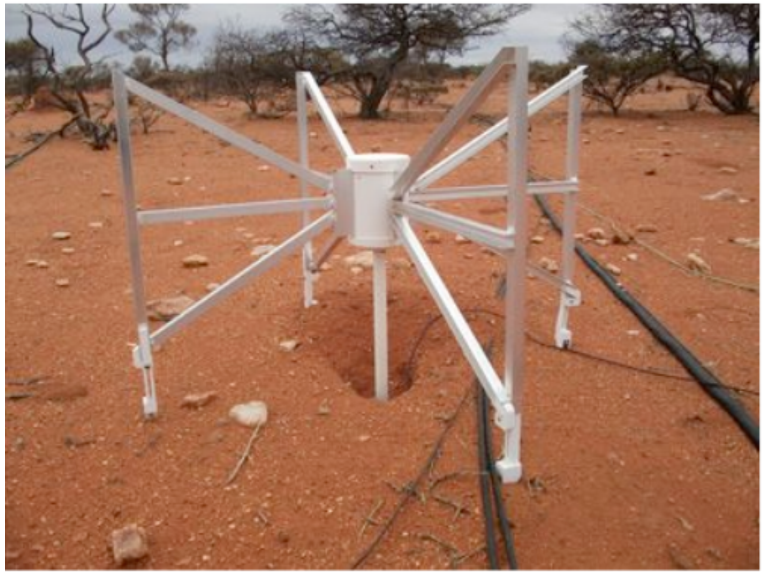

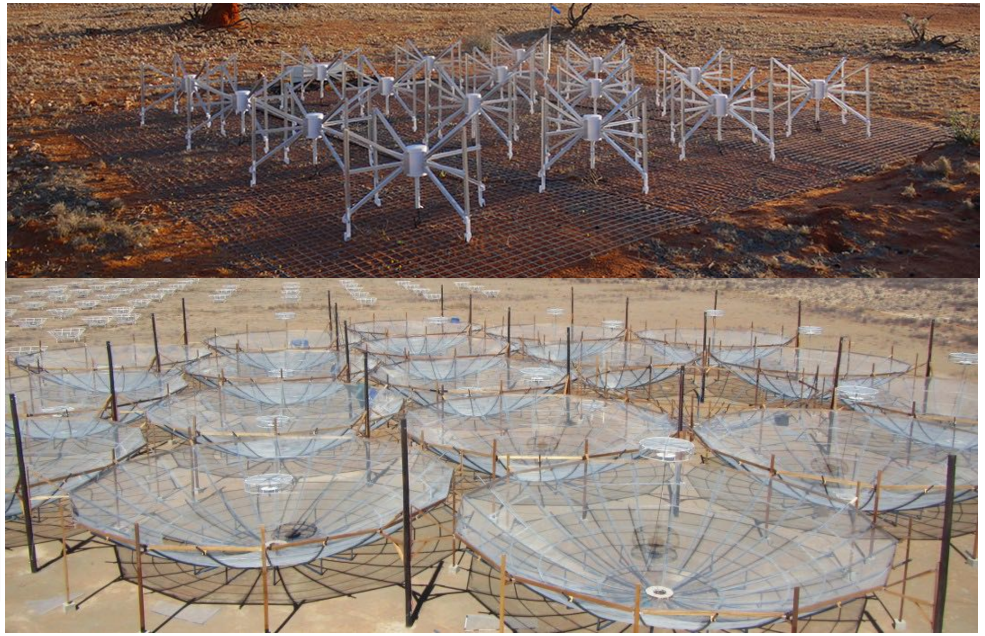

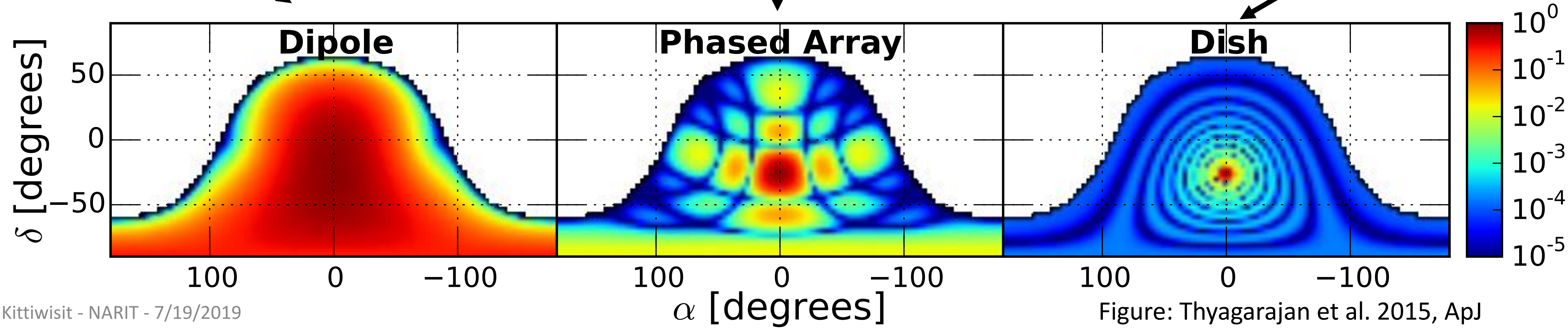

Figure: Thyagarajan et al. 2015, ApJ

Challenges #2: Foreground is extremely bright and must be mitigated

Figure: Zaroubi 2012

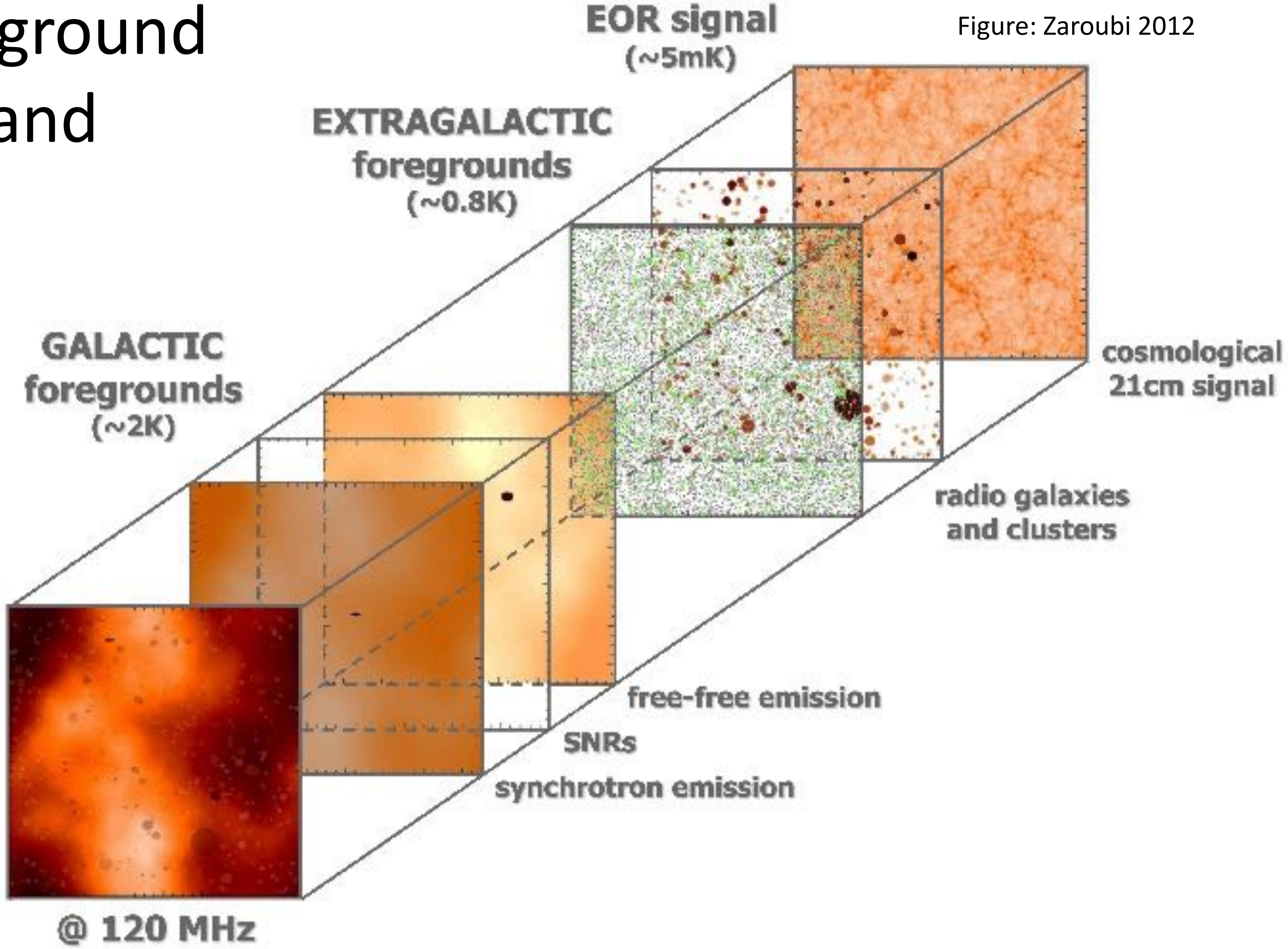

Current detection efforts are statistical primarily through 21 cm power spectrum

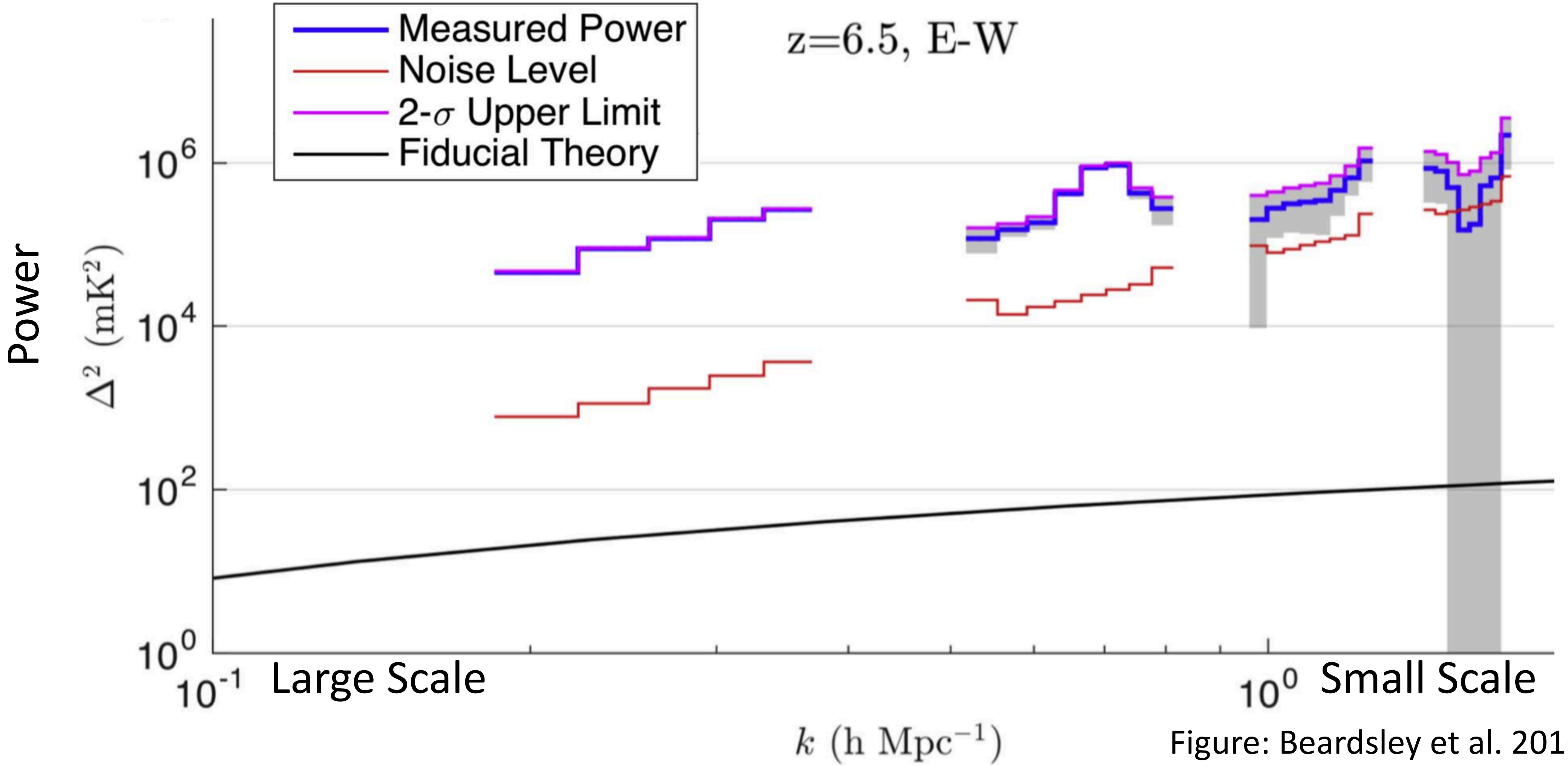

Figure: Beardsley et al. 2016, MNRAS

Current State of the Field - Averaged Power Spectrum

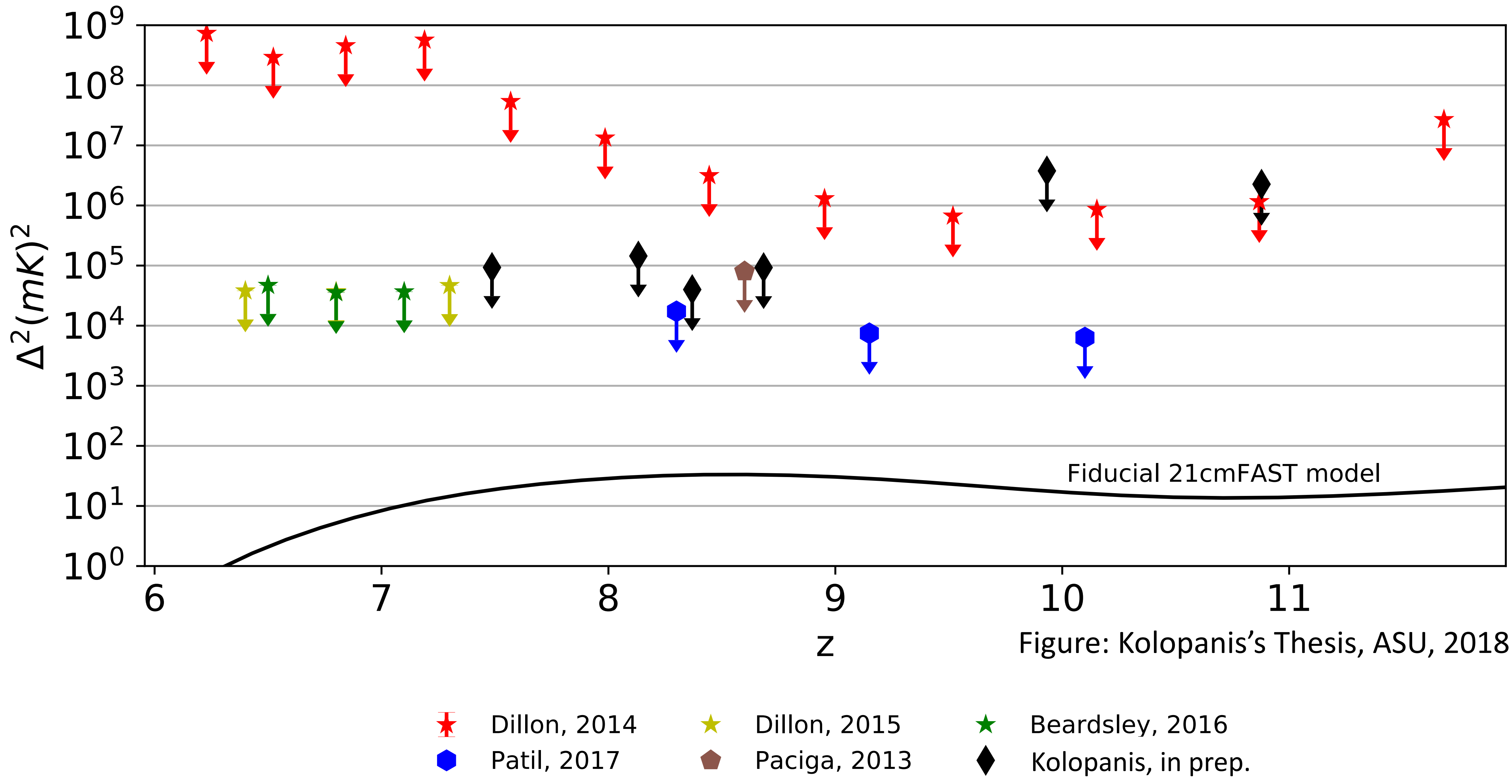

Figure: Kolopanis's Thesis, ASU, 2018

Global 21 cm experiments aim to measure the sky-averaged 21 cm spectrum from EoR/CD

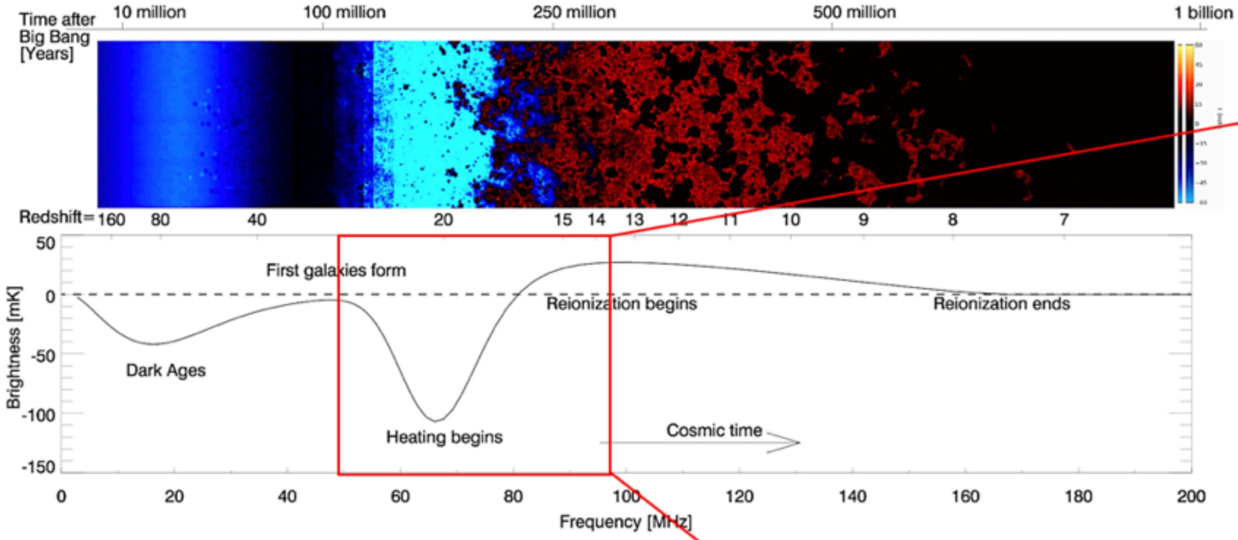

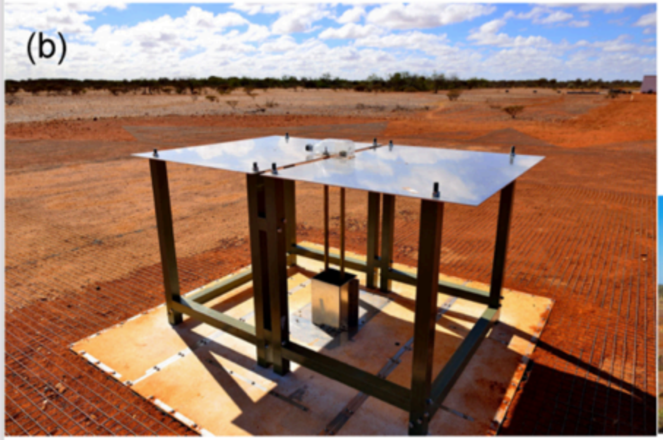

Experiment to Detect the Global Epoch of Reionization Signature (EDGES)

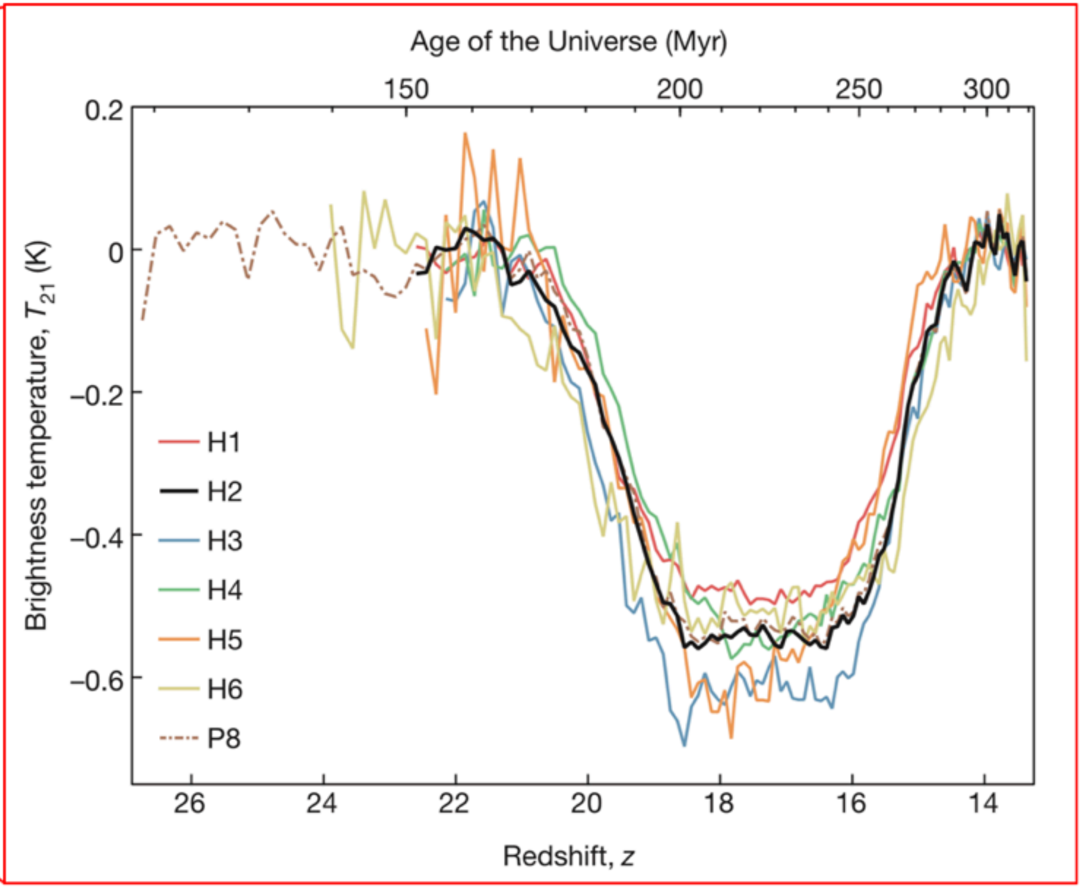

Bowman et al. 2018, Nature, 555, 67–70

Part I - Summary

- 21 cm lines can be used to probe neutral hydrogen gas during reionization and Cosmic Dawn eras to study formation and evolution of the first stars and galaxies
- It can be done with a radio interferometer in meter wavelengths
- It is very challenging due to complex instruments and bright foreground
- Statistical analysis will be important for the next decade

A power spectrum can only describes a Gaussian signal - EoR is not Gaussian

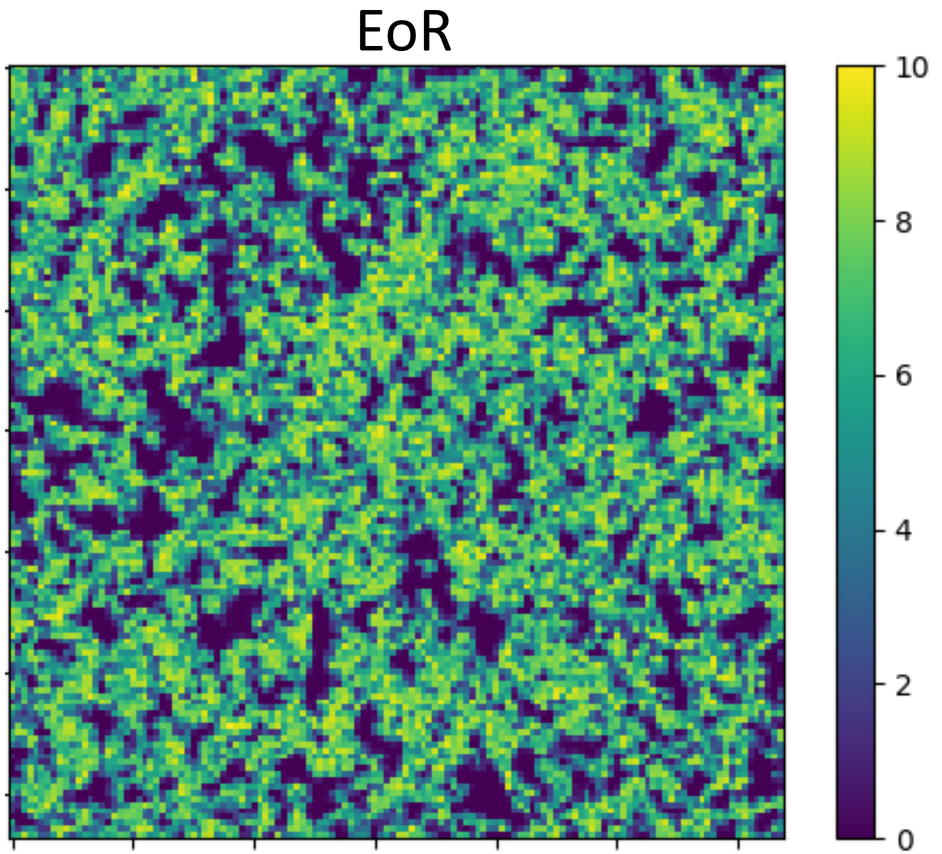

Lidz & Malloy 2014

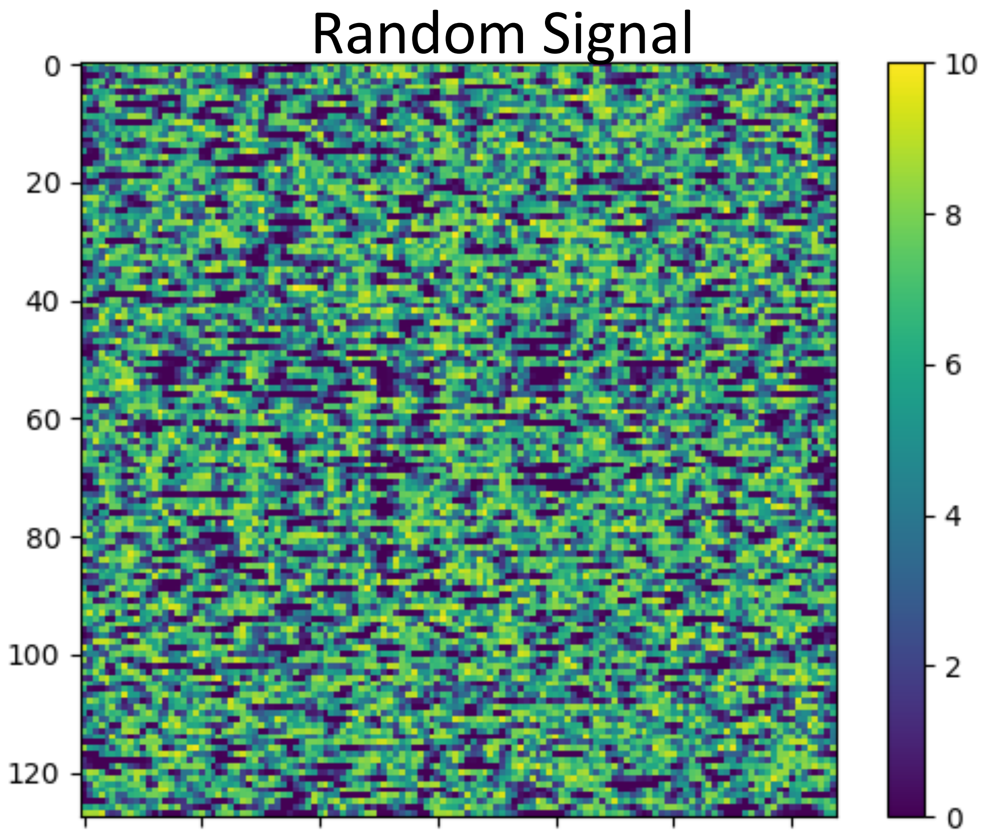

Random signal with the same variance as the EoR signal will have the same power spectrum

Probability Distribution Function (PDF) and One-point statistics

- PDF: histogram of a map normalized to integral of one
- Variance (2^{nd} order) describes the spread
- Skewness (3^{rd} order) describes the symmetry
    - Positive = tail above mean
    - Negative = tail below mean
- Kurtosis (4^{th} order) describe tailedness
    - Positive = more tails
    - Negative = less tails
- A perfect Gaussian has zero skewness and kurtosis

- Mathematically, one-point statistics are standardization of statistical moments

$$m_p = \frac{1}{N}\sum_{i=0}^{N}(x-\bar{x})^p$$

$$\text{variance} = m_2$$

$$\text{skewness} = \frac{m_3}{m_2^{(3/2)}}$$

$$\text{kurtosis} = \frac{m_4}{m_2^2} - 3$$

30% Ionized

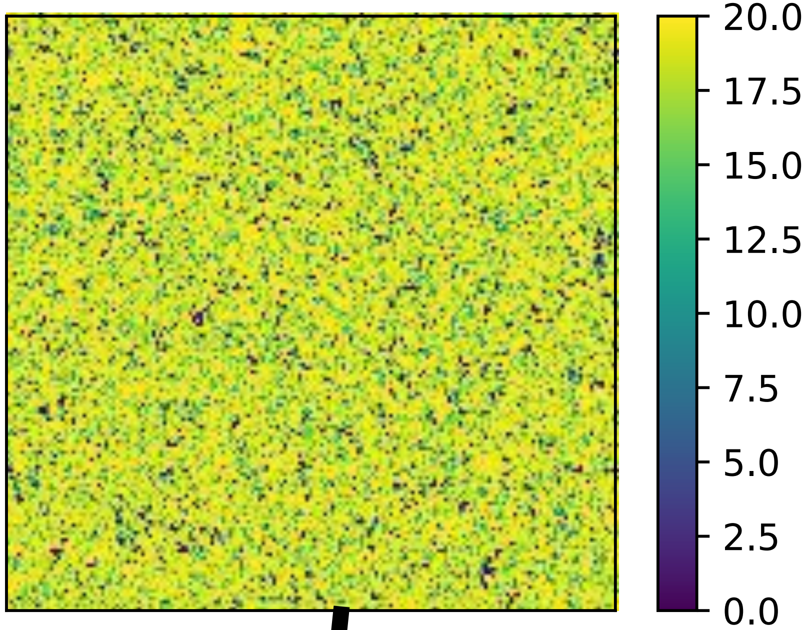

- Gaussian-like peak with a long left tail
- Negative skewness
- Positive kurtosis

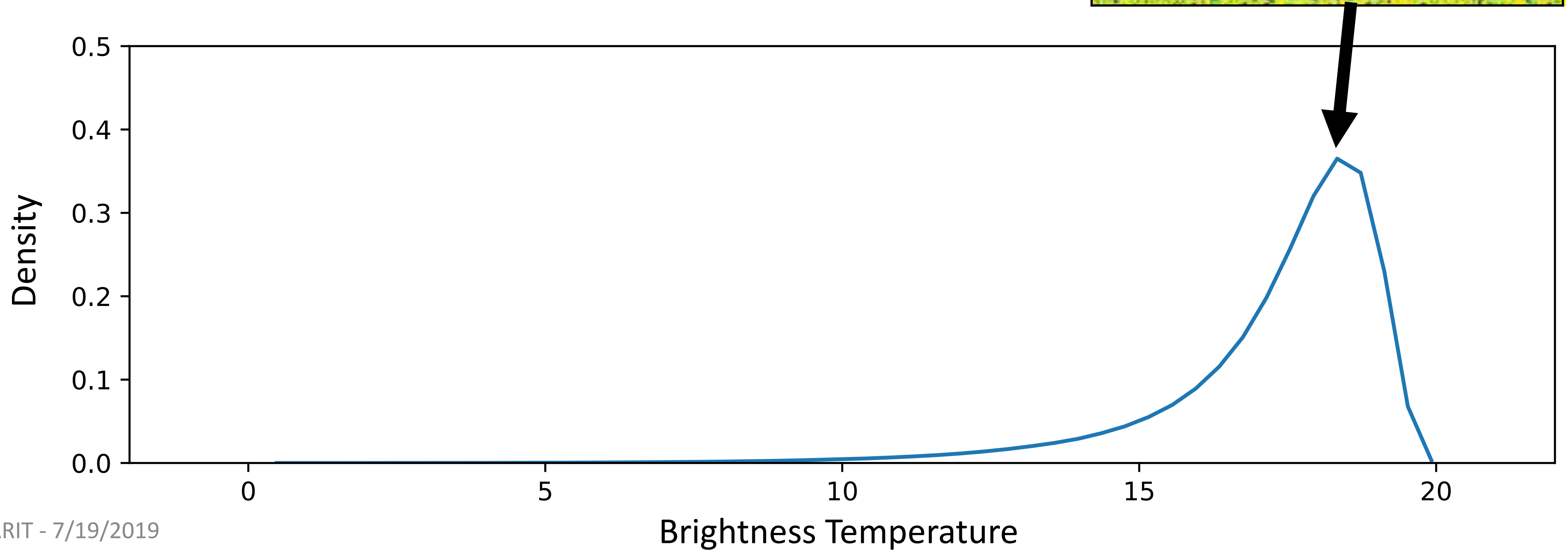

- Bi-modal PDF (twin-peaks PDF)
- High variance
- Negative kurtosis

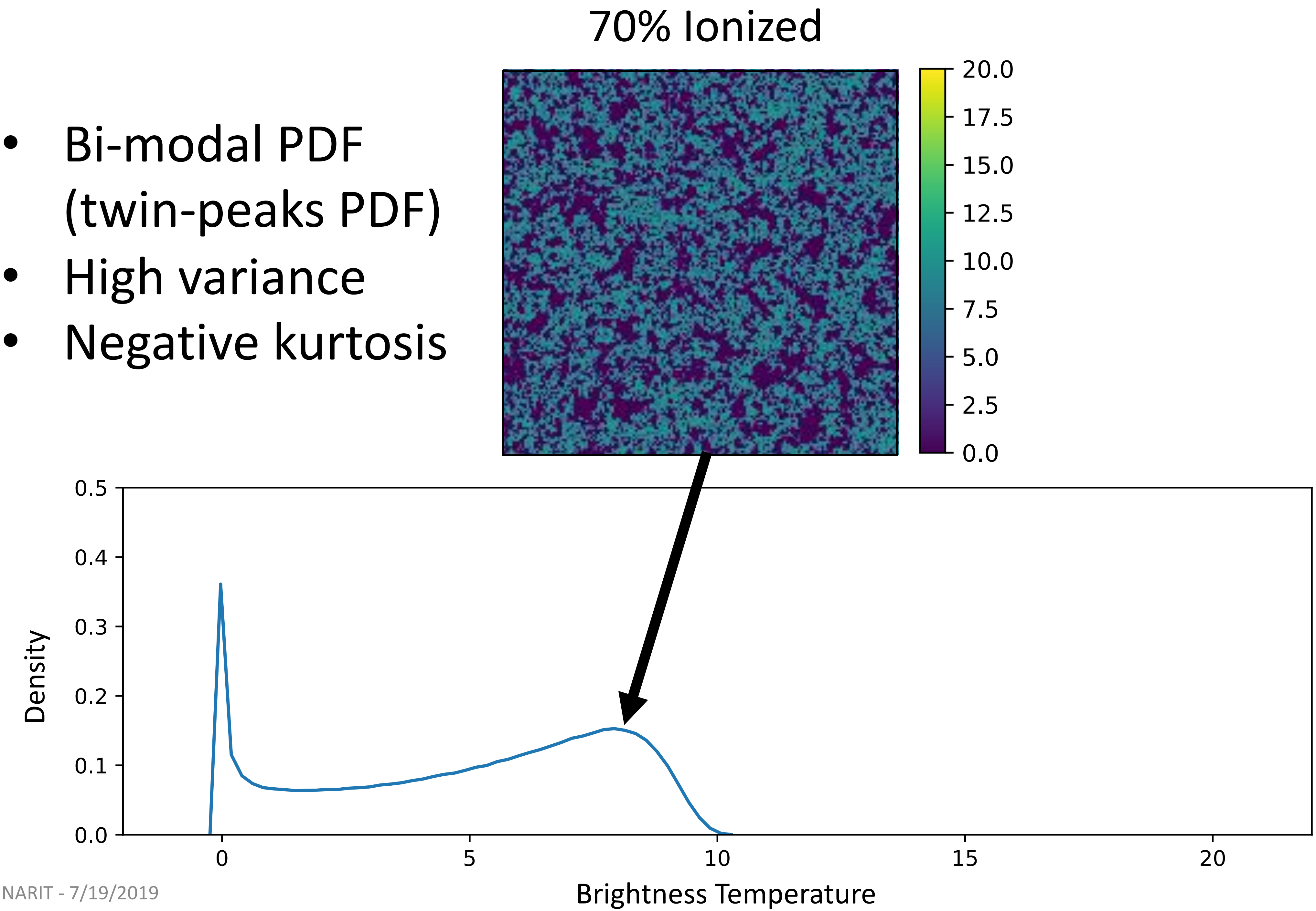

95% Ionized

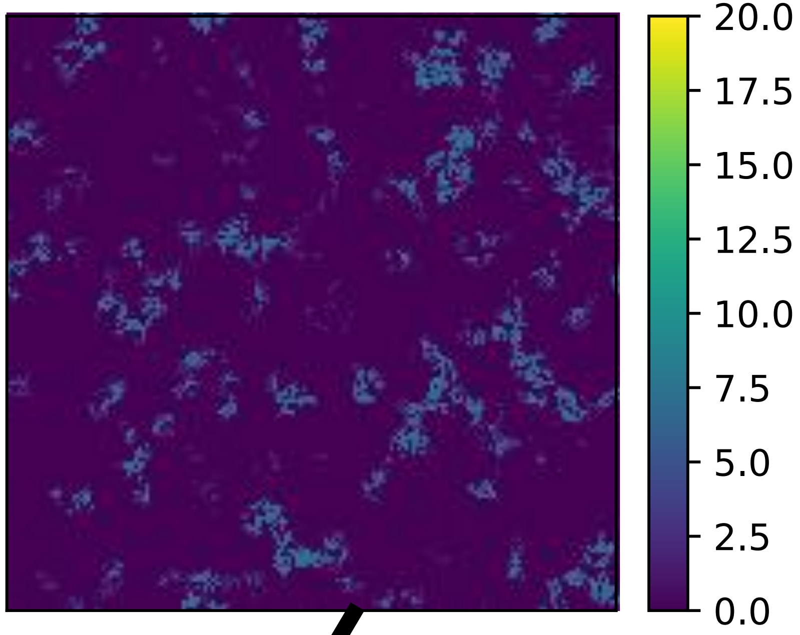

- Delta-function-like PDF
- Positive skewness
- Positive kurtosis

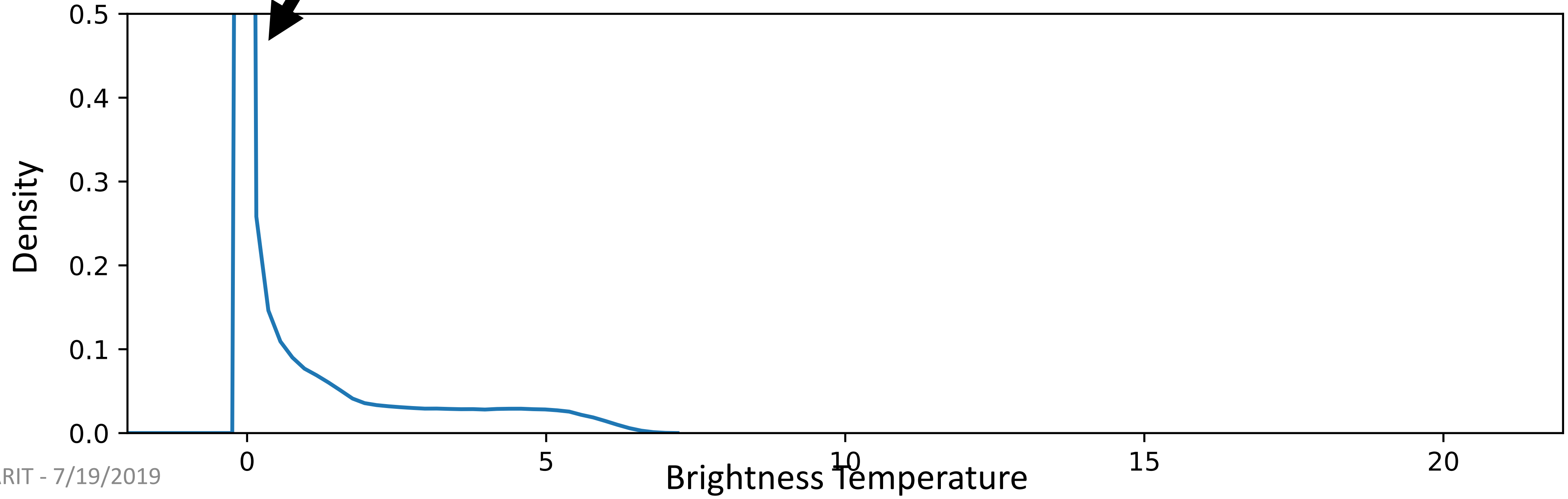

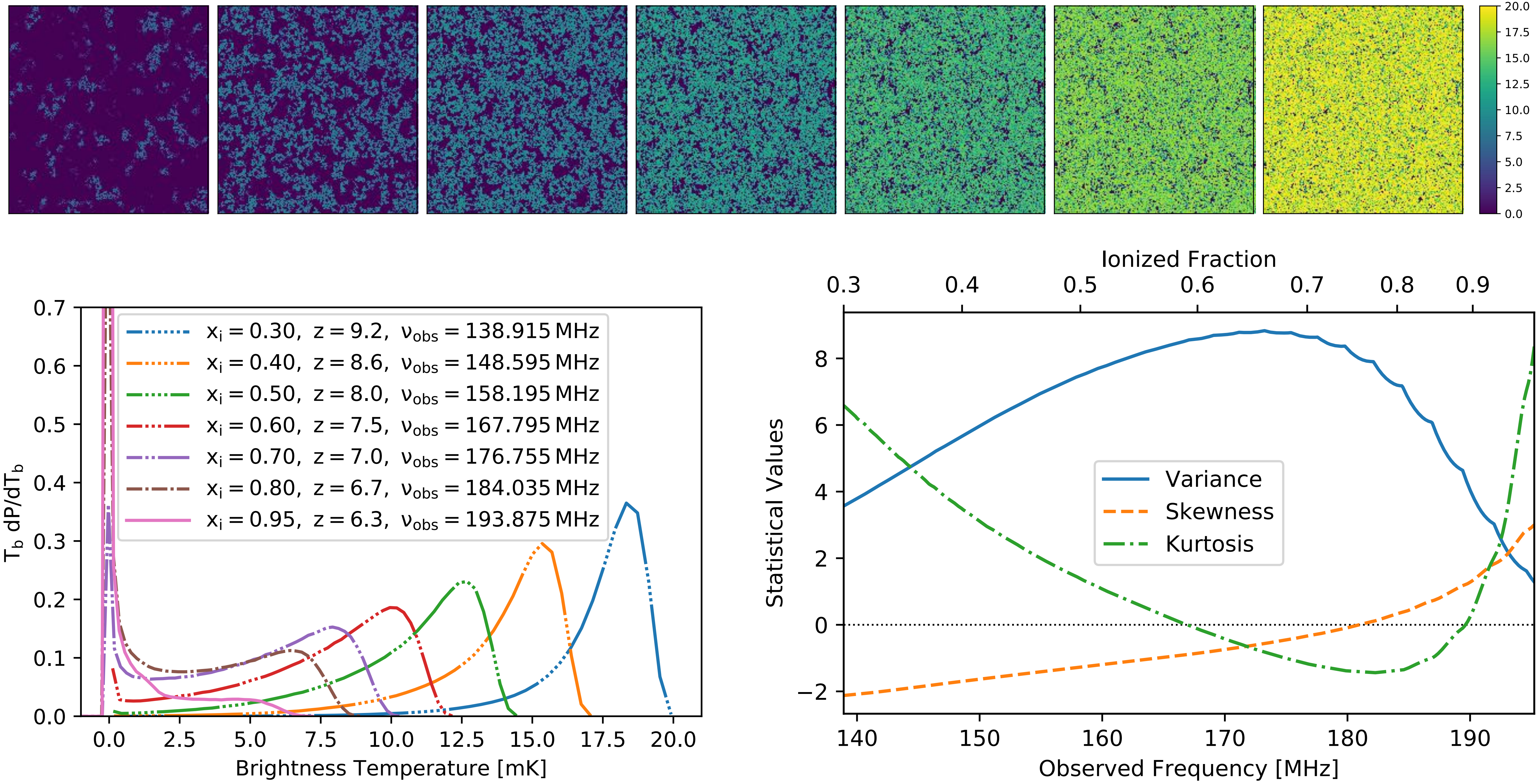
20.0
17.5
15.0
12.5
10.0
7.5
5.0
2.5
0.0
$x_i = 0.30,\ z = 9.2,\ \nu_{obs} = 138.915\,\mathrm{MHz}$
$x_i = 0.40,\ z = 8.6,\ \nu_{obs} = 148.595\,\mathrm{MHz}$
$x_i = 0.50,\ z = 8.0,\ \nu_{obs} = 158.195\,\mathrm{MHz}$
$x_i = 0.60,\ z = 7.5,\ \nu_{obs} = 167.795\,\mathrm{MHz}$
$x_i = 0.70,\ z = 7.0,\ \nu_{obs} = 176.755\,\mathrm{MHz}$
$x_i = 0.80,\ z = 6.7,\ \nu_{obs} = 184.035\,\mathrm{MHz}$
$x_i = 0.95,\ z = 6.3,\ \nu_{obs} = 193.875\,\mathrm{MHz}$
$T_b\,dP/dT_b$
0.0
0.1
0.2
0.3
0.4
0.5
0.6
0.7
0.0
2.5
5.0
7.5
10.0
12.5
15.0
17.5
20.0
Brightness Temperature [mK]
Ionized Fraction
0.3
0.4
0.5
0.6
0.7
0.8
0.9
Statistical Values
8
6
4
2
0
−2
Variance
Skewness
Kurtosis
140
150
160
170
180
190
Observed Frequency [MHz]

Sensitivity Analysis of 21 cm One-point Statistics for HERA

- Utilize realistic mock observation pipeline
  - Variance, skewness and kurtosis
  - Full-sky 21 cm inputs
  - HERA as the instrument model
  - Thermal noise
  - Sample variance
  - Drift scan observation
  - Frequency bandwidth averaging
  - Assume perfect foreground removal and foreground avoiding regimes
- Kittiwisit et al. 2018, MNRAS, arXiv:1708.00036

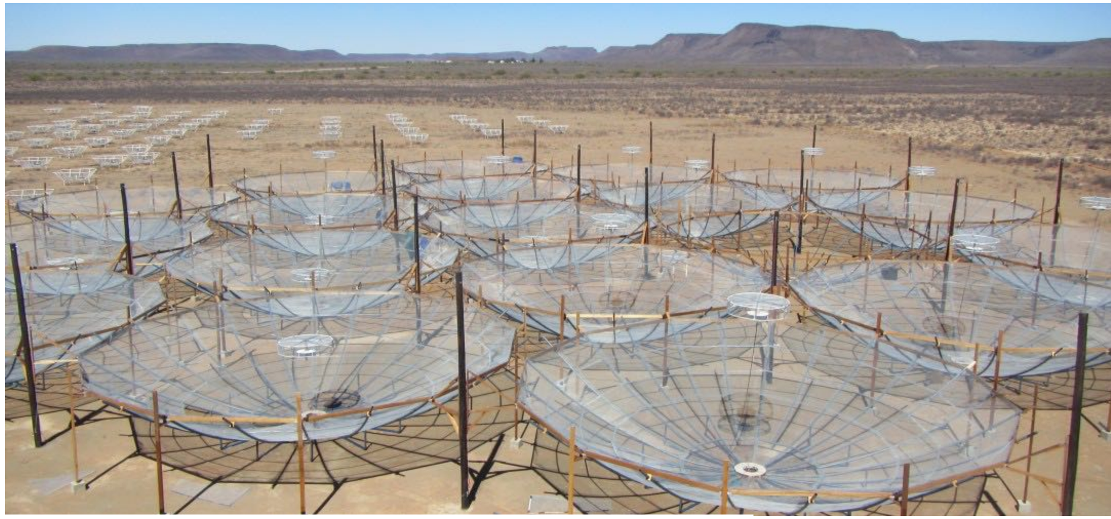

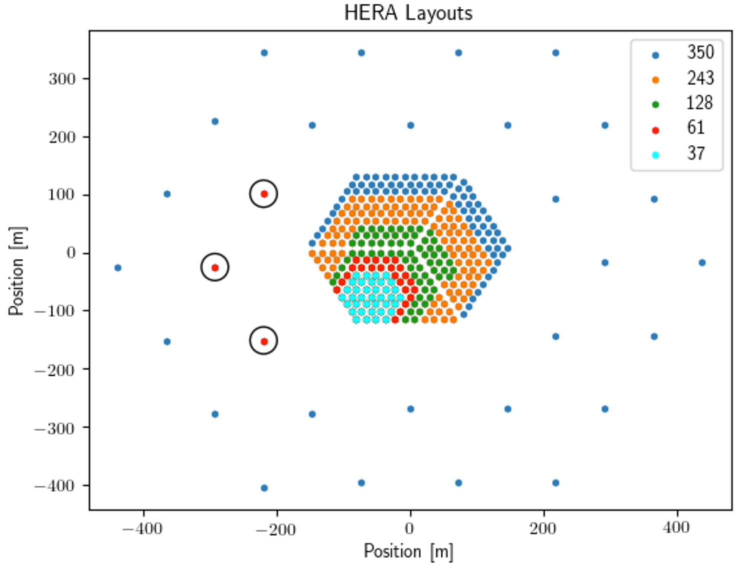

HERA Mock Observation Pipeline (No Foreground)

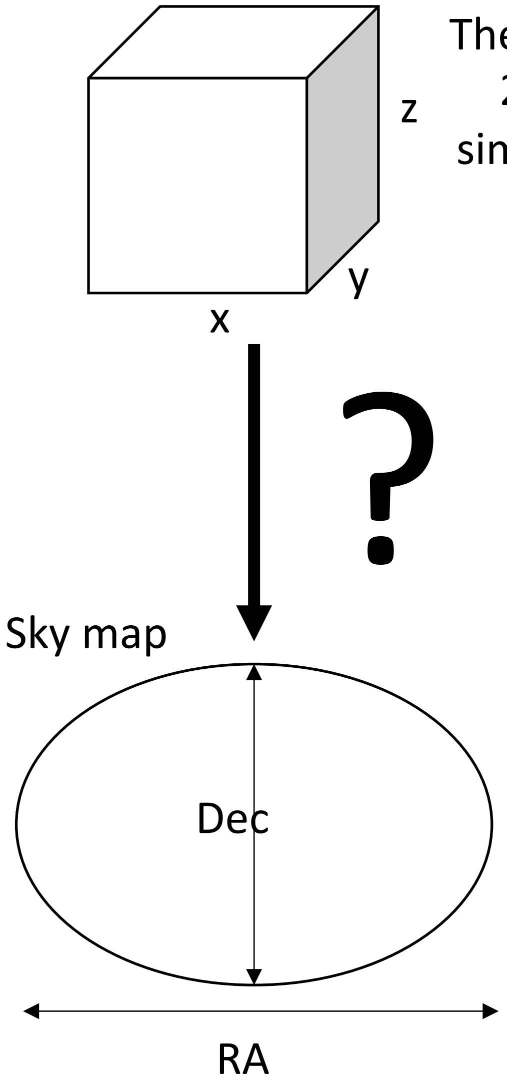

Theoretical
21 cm
simulation
cube

HERA Mock Observation Pipeline (No Foreground)

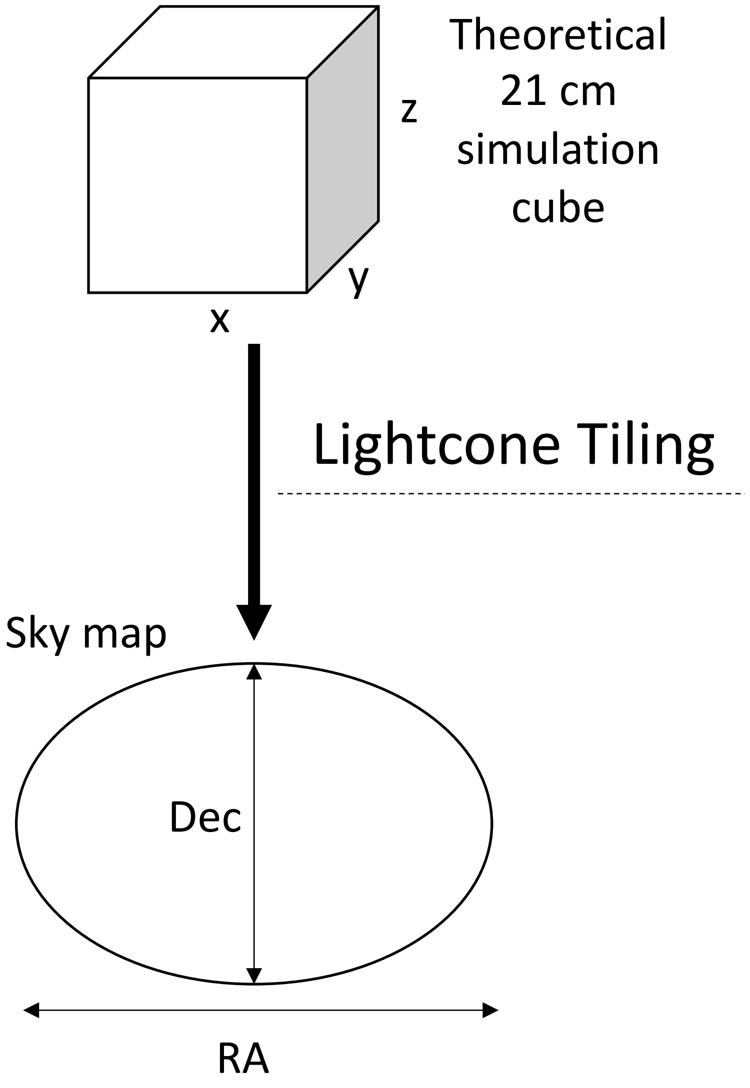

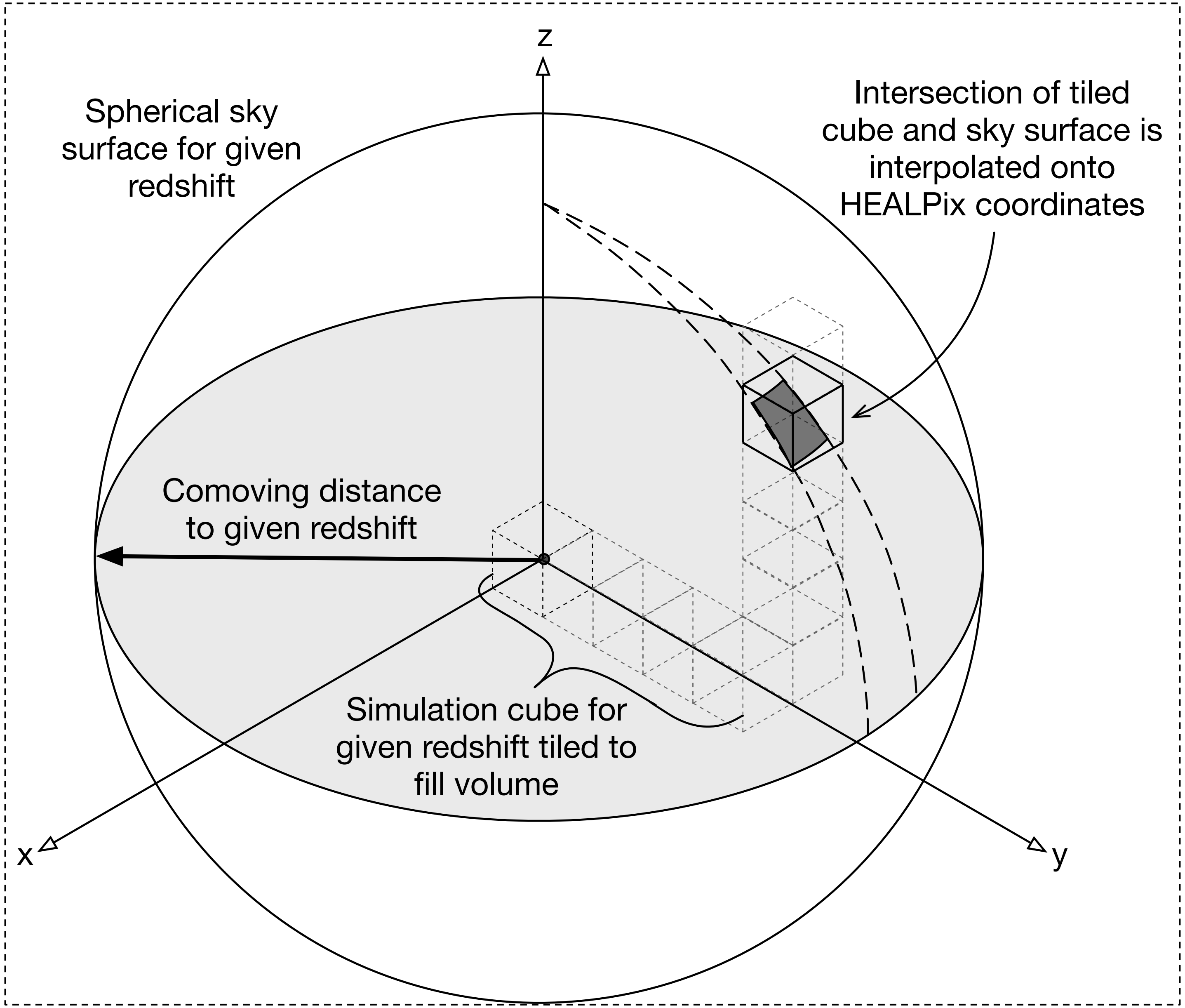

HERA Mock Observation Pipeline (No Foreground)

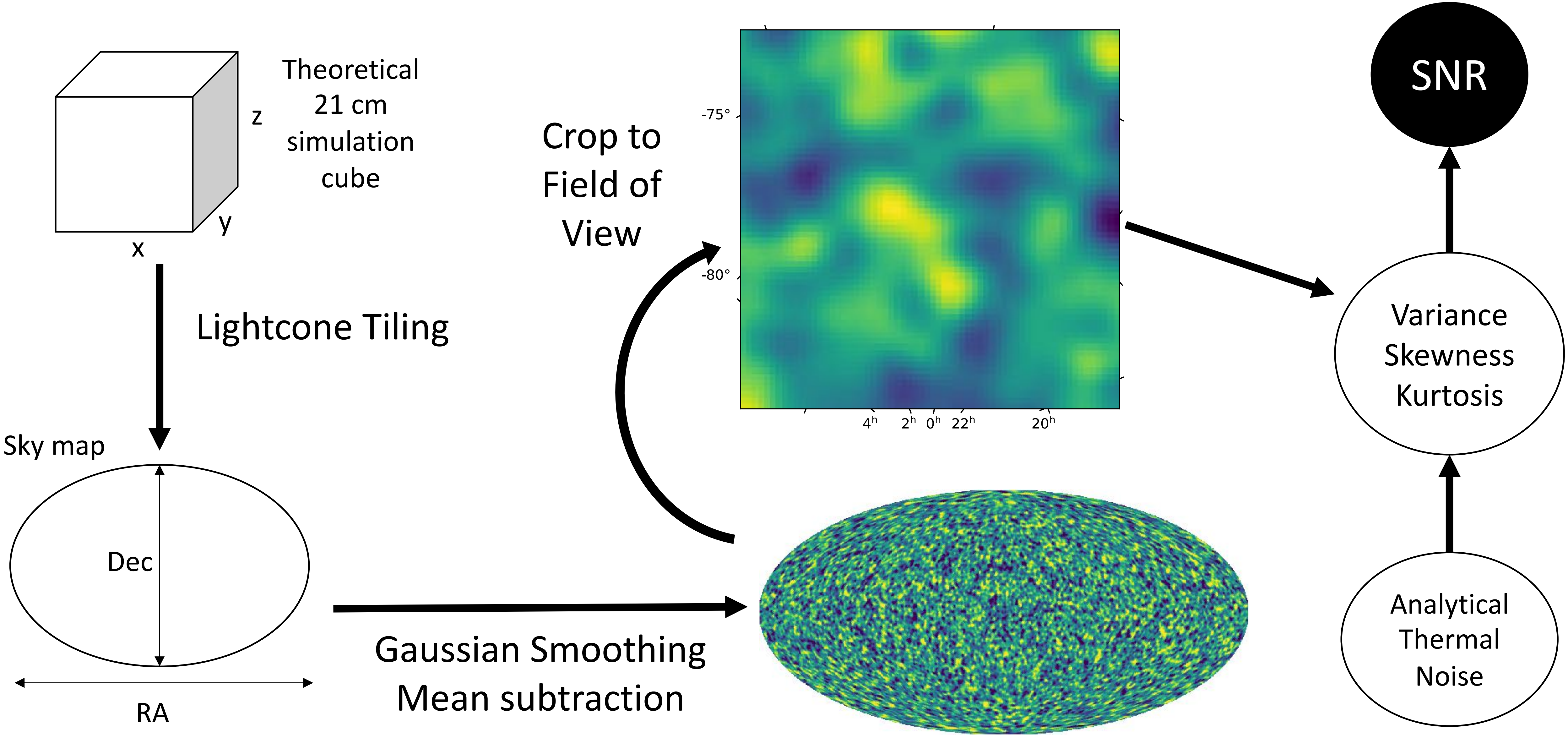

Simulated Intensity Maps

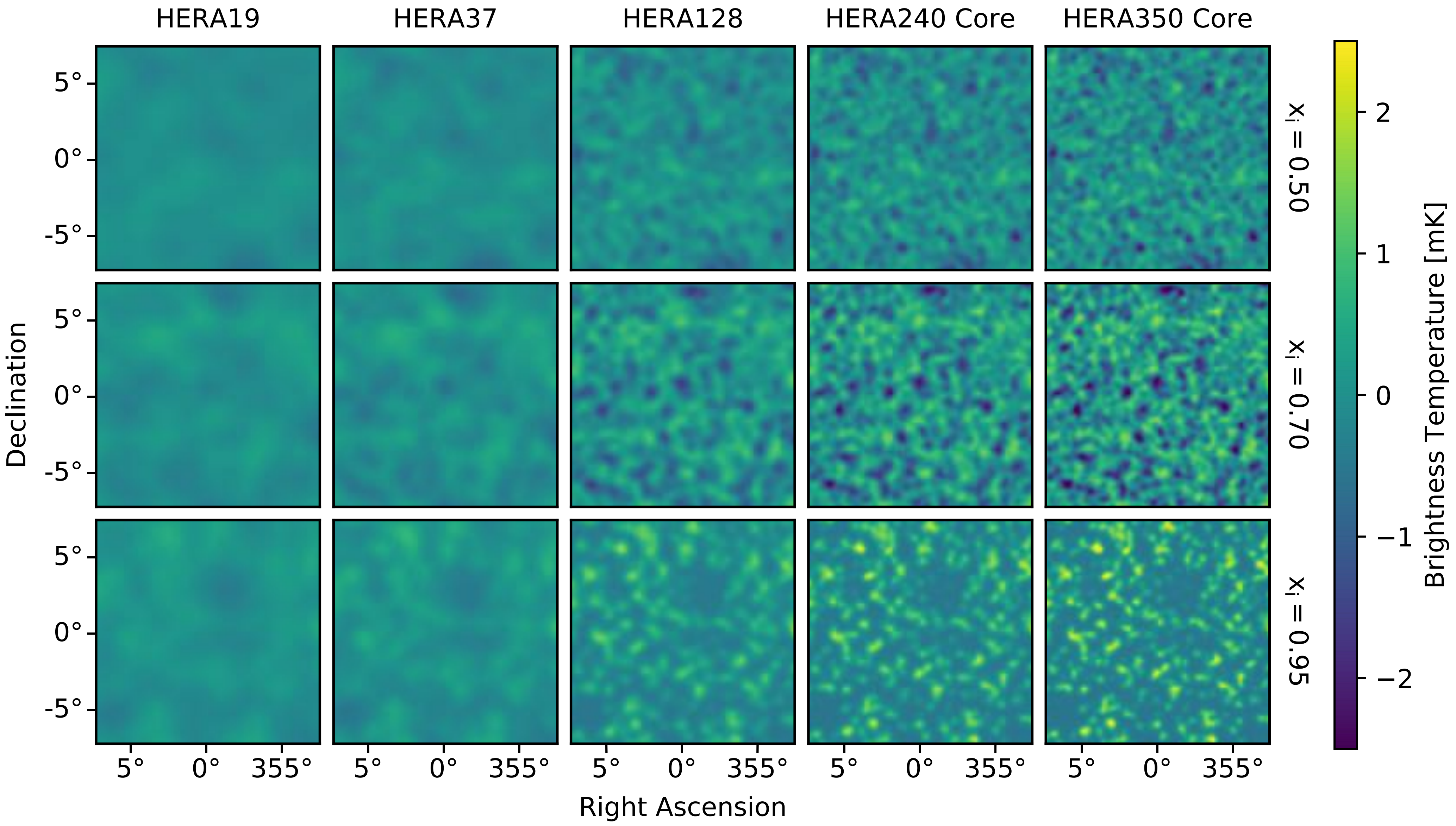

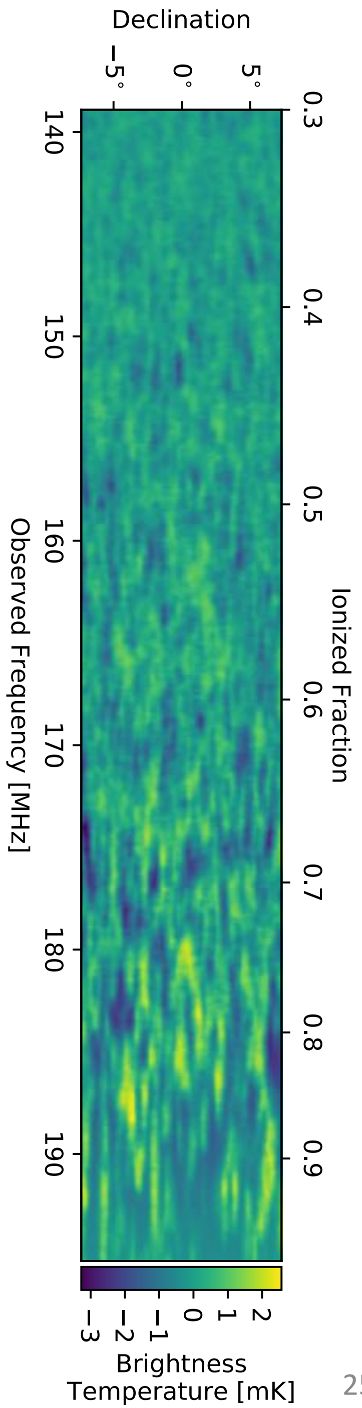

Analytical Thermal Noise Uncertainty

- Expanded from Watkinson & Pritchard 2014 to kurtosis
- 100 hours of integration, approximately 1 year

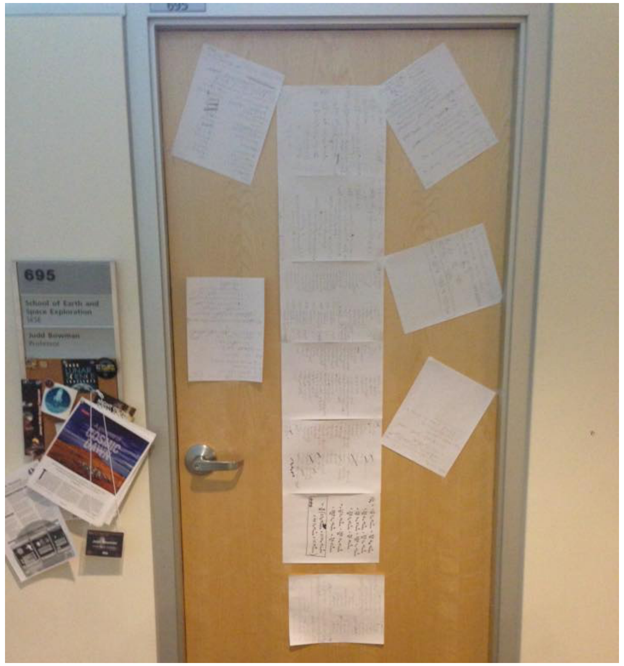

$\langle n_i \rangle$	$=0$	
$\langle n_i n_j \rangle$	$\langle n_i^2 \rangle = \sigma_i^2 \quad (i=j)$ $\langle n_i \rangle \langle n_j \rangle = 0 \quad (i \neq j)$	$\delta_{ij}\sigma_j^2$
$\langle n_i n_j^2 \rangle$	$\langle n_i^3 \rangle = 0 \quad (i=j)$ $\langle n_i \rangle \langle n_j^2 \rangle = 0 \quad (i \neq j)$	0
$\langle n_i^2 n_j^2 \rangle$	$\langle n_i^4 \rangle = 3\sigma_i^4 \quad (i=j)$ $\langle n_i^2 \rangle \langle n_j^2 \rangle = \sigma_i^2\sigma_j^2 \quad (i \neq j)$	$(1+2\delta_{ij})\sigma_i^2\sigma_j^2$
$\langle n_i^2 n_j^3 \rangle$	$\langle n_i^5 \rangle = 0 \quad (i=j)$ $\langle n_i^2 \rangle \langle n_j^3 \rangle = 0 \quad (i \neq j)$	0
$\langle n_i n_j^3 \rangle$	$\langle n_i^4 \rangle = 3\sigma_i^4 \quad (i=j)$ $\langle n_i \rangle \langle n_j^3 \rangle = 0 \quad (i \neq j)$	$3\delta_{ij}\sigma_i^4$
$\langle n_i^3 n_j^3 \rangle$	$\langle n_i^6 \rangle = 15\sigma_i^6 \quad (i=j)$ $\langle n_i^3 \rangle \langle n_j^3 \rangle = 0 \quad (i \neq j)$	$15\delta_{ij}\sigma_i^6$

$\langle n_i n_j^4 \rangle$	$\langle n_i^5 \rangle = 0 \quad (i=j)$ $\langle n_i \rangle \langle n_j^4 \rangle = 0 \quad (i \neq j)$	0
$\langle n_i^2 n_j^4 \rangle$	$\langle n_i^6 \rangle = 15\sigma_i^6 \quad (i=j)$ $\langle n_i^2 \rangle \langle n_j^4 \rangle = 3\sigma_i^2\sigma_j^4 \quad (i \neq j)$	$(3+12\delta_{ij})\sigma_i^2$
$\langle n_i^3 n_j^4 \rangle$	$\langle n_i^7 \rangle = 0 \quad (i=j)$ $\langle n_i^3 \rangle \langle n_j^4 \rangle = 0 \quad (i \neq j)$	0
$\langle n_i^4 n_j^4 \rangle$	$\langle n_i^8 \rangle = 105\sigma_i^8 \quad (i=j)$ $\langle n_i^4 \rangle \langle n_j^4 \rangle = 9\sigma_i^4\sigma_j^4 \quad (i \neq j)$	$(9+96\delta_{ij})\sigma_i^4$

skewness, and $X = m_2$ and $Y = m_4$ for kurtosis.

Equations A9 to A14 summarize results from Watkinson & Pritchard (2014). Here, σ_i is assumed to be equal to σ_{noise} in Equation 7 for all pixels.

$$\hat{m}_2 = \frac{1}{N_{pix}} \sum_{i=0}^{N_{pix}} (\delta T_i - \overline{\delta T})^2 - \sigma_{noise}^2, \tag{A9}$$

$$\hat{m}_3 = \frac{1}{N_{pix}} \sum_{i=0}^{N_{pix}} (\delta T_i - \overline{\delta T})^3, \tag{A10}$$

$$C_{\hat{m}_2\hat{m}_3} = \frac{6}{N_{pix}} m_3 \sigma_{noise}^2, \tag{A11}$$

$$V_{\hat{m}_2} = V_{Var} = \frac{2}{N_{pix}} (2m_2\sigma_{noise}^2 + \sigma_{noise}^4), \tag{A12}$$

$$V_{\hat{m}_3} = \frac{3}{N_{pix}} (3m_4\sigma_{noise}^2 + 12m_2\sigma_{noise}^4 + 5\sigma_{noise}^6), \tag{A13}$$

$$V_{S_3} \approx \frac{1}{(m_2)^3} V_{\hat{m}_3} + \frac{9}{4}\frac{(m_3)^2}{(m_2)^5} V_{\hat{m}_2} - 3\frac{m_3}{(m_2)^4} C_{\hat{m}_2\hat{m}_3}. \tag{A14}$$

We follow the procedure in Watkinson & Pritchard (2014) and are able to confirm their results. In addition, we derive the estimator variance for kurtosis as follows.

First the the 4th moment with added noise is constructed.

$$\begin{aligned} \hat{m}_4^{test} &= \frac{1}{N_{pix}} \sum_{i=0}^{N_{pix}} (x_i - \overline{x})^4 \\ &= \frac{1}{N_{pix}} \sum_{i=0}^{N_{pix}} [(\delta T_i - \overline{\delta T}) + n_i]^4. \end{aligned} \tag{A15}$$

Then, we average over the noise.

$$\begin{aligned} \langle \hat{m}_4^{test} \rangle &= \frac{1}{N_{pix}} \sum_{i=0}^{N_{pix}} [(\delta T_i - \overline{\delta T})^4 + 4(\delta T_i - \overline{\delta T})^3 \langle n_i \rangle \\ &\quad + 6(\delta T_i - \overline{\delta T})^2 \langle n_i^2 \rangle + 4(\delta T_i - \overline{\delta T}) \langle n_i^3 \rangle + \langle n_i^4 \rangle] \\ &= \frac{1}{N_{pix}} \sum_{i=0}^{N_{pix}} (\delta T_i - \overline{\delta T})^4 \\ &\quad + 6 \frac{1}{N_{pix}} \sum_{i=0}^{N_{pix}} (\delta T_i - \overline{\delta T})^2 \sigma_i^2 + 3\sigma_i^4 \\ &= \frac{1}{N_{pix}} \sum_{i=0}^{N_{pix}} (\delta T_i - \overline{\delta T})^4 \\ &\quad + 6m_2\sigma_{noise}^2 + 3\sigma_{noise}^4. \end{aligned} \tag{A16}$$

This implies that the unbiased estimator of the 4th moment is,

$$\begin{aligned} \hat{m}_4 &= \frac{1}{N_{pix}} \sum_{i=0}^{N_{pix}} (\delta T_i - \overline{\delta T})^4 - 6m_2\sigma_{noise}^2 - 3\sigma_{noise}^4 \\ &= \frac{1}{N_{pix}} \sum_{i=0}^{N_{pix}} (\delta T_i - \overline{\delta T})^4 - \frac{3}{2} N_{pix} V_{\hat{m}_2}. \end{aligned} \tag{A17}$$

Next we derive the estimator variance of the 4th moment. We substitute $\mu_i = \delta T_i - \overline{\delta T}$ and $\kappa = 3N_{pix}V_{\hat{m}_2}/2$ to simplify the derivation.

$$\begin{aligned} V_{\hat{m}_4} = \Big\langle &\frac{1}{N_{pix}^2} \sum_{i=0}^{N_{pix}} \sum_{j=0}^{N_{pix}} [(\mu_i + n_i)^4 - \kappa] \\ &\times [(\mu_j + n_j)^4 - \kappa] \Big\rangle - (m_4)^2. \end{aligned} \tag{A18}$$

Expanding this expression and moving the noise averaging brackets inside the summation gives,

$$\begin{aligned} V_{\hat{m}_4} =& \frac{1}{N_{pix}^2} \sum_{i=0}^{N_{pix}} \sum_{j=0}^{N_{pix}} \Big[\mu_i^4\mu_j^4 + 4\mu_i^4\mu_j^3\langle n_j \rangle \\ &+ 6\mu_i^4\mu_j^2\langle n_j^2 \rangle + 4\mu_i^4\mu_j\langle n_j^3 \rangle + \mu_i^4\langle n_j^4 \rangle - \kappa\mu_i^4 \\ &+ 4\mu_i^3\mu_j^4\langle n_i \rangle + 16\mu_i^3\mu_j^3\langle n_i n_j \rangle + 24\mu_i^3\mu_j^2\langle n_i n_j^2 \rangle \\ &+ 16\mu_i^3\mu_j\langle n_i n_j^3 \rangle + 4\mu_i^3\langle n_i n_j^4 \rangle - 4\kappa\mu_i^3\langle n_i \rangle \\ &+ 6\mu_i^2\mu_j^4\langle n_i^2 \rangle + 24\mu_i^2\mu_j^3\langle n_i^2 n_j \rangle + 36\mu_i^2\mu_j^2\langle n_i^2 n_j^2 \rangle \\ &+ 24\mu_i^2\mu_j\langle n_i^2 n_j^3 \rangle + 6\mu_i^2\langle n_i^2 n_j^4 \rangle - 6\kappa\mu_i^2\langle n_i^2 \rangle \\ &+ 4\mu_i\mu_j^4\langle n_i^3 \rangle + 16\mu_i\mu_j^3\langle n_i^3 n_j \rangle + 24\mu_i\mu_j^2\langle n_i^3 n_j^2 \rangle \\ &+ 16\mu_i\mu_j\langle n_i^3 n_j^3 \rangle + 4\mu_i\langle n_i^3 n_j^4 \rangle - 4\kappa\mu_i\langle n_i^3 \rangle \\ &+ \mu_j^4\langle n_i^4 \rangle + 4\mu_j^3\langle n_i^4 n_j \rangle + 6\mu_j^2\langle n_i^4 n_j^2 \rangle \\ &+ 4\mu_j\langle n_i^4 n_j^3 \rangle + \langle n_i^4 n_j^4 \rangle - \kappa\langle n_i^4 \rangle \\ &- \kappa\mu_j^4 - 4\kappa\mu_j^3\langle n_j \rangle - 6\kappa\mu_j^2\langle n_j^2 \rangle - 4\kappa\mu_j\langle n_j^3 \rangle \\ &- \kappa\langle n_j^4 \rangle + \kappa^2 \Big] - (m_4)^2. \end{aligned} \tag{A19}$$

Using the Gaussian noise identities reduces the expression to,

$$\begin{aligned} V_{\hat{m}_4} =& \frac{1}{N_{pix}^2} \sum_{i=0}^{N_{pix}} \sum_{j=0}^{N_{pix}} \Big[\mu_i^4\mu_j^4 + 6\mu_i^4\mu_j^2\sigma_j^2 + 3\mu_i^4\sigma_j^4 - \kappa\mu_i^4 \\ &+ 16\mu_i^3\mu_j^3\delta_{ij}\sigma_j^2 + 48\mu_i^3\mu_j\delta_{ij}\sigma_i^4 + 6\mu_i^2\mu_j^4\sigma_i^2 \\ &+ 36\mu_i^2\mu_j^2(1+2\delta_{ij})\sigma_i^2\sigma_j^2 + 6\mu_i^2(3+12\delta_{ij})\sigma_i^2\sigma_j^4 \\ &- 6\kappa\mu_i^2\sigma_i^2 + 48\mu_i\mu_j^3\delta_{ij}\sigma_j^4 + 240\mu_i\mu_j\delta_{ij}\sigma_i^6 \\ &+ 3\mu_j^4\sigma_i^4 + 6\mu_j^2(3+12\delta_{ij})\sigma_i^4\sigma_j^2 + (9+96\delta_{ij})\sigma_i^4\sigma_j^4 \\ &- 3\kappa\sigma_i^4 - \kappa\mu_j^4 - 6\kappa\mu_j^2\sigma_j^2 - 3\kappa\sigma_j^4 + \kappa^2 \Big] \\ &- (m_4)^2. \end{aligned} \tag{A20}$$

Doing the summation to perform index conversion via δ_{ij}, substituting all $\frac{1}{N_{pix}}\sum_{i=0}^{N_{pix}} \mu_i^k$ terms with the p-th moments m_p and σ_i with σ_{noise}, re-substituting $\kappa = 3N_{pix}V_{\hat{m}_2}/2 = 6m_2\sigma_{noise}^2 + 3\sigma_{noise}^4$, and cancelling out many terms will yield the estimator variance of the 4th moment,

$$\begin{aligned} V_{\hat{m}_4} = \frac{8}{N_{pix}} (&2m_6\sigma_{noise}^2 + 21m_4\sigma_{noise}^4 \\ &+ 48m_2\sigma_{noise}^6 + 12\sigma_{noise}^8). \end{aligned} \tag{A21}$$

The estimator covariance between 2nd and 4th moment

HERA350 Core Measurement (80 kHz channel, 1 year noise)

- Strong fluctuations in measurements from a single field due to sample variance
- Averaging over 20 measurements from different fields in the HERA drift scan recovers statistics of the sky model
- Thermal noise dominate skewness and kurtosis at low frequency
    - But measurements are possible at higher frequency (where it matters)

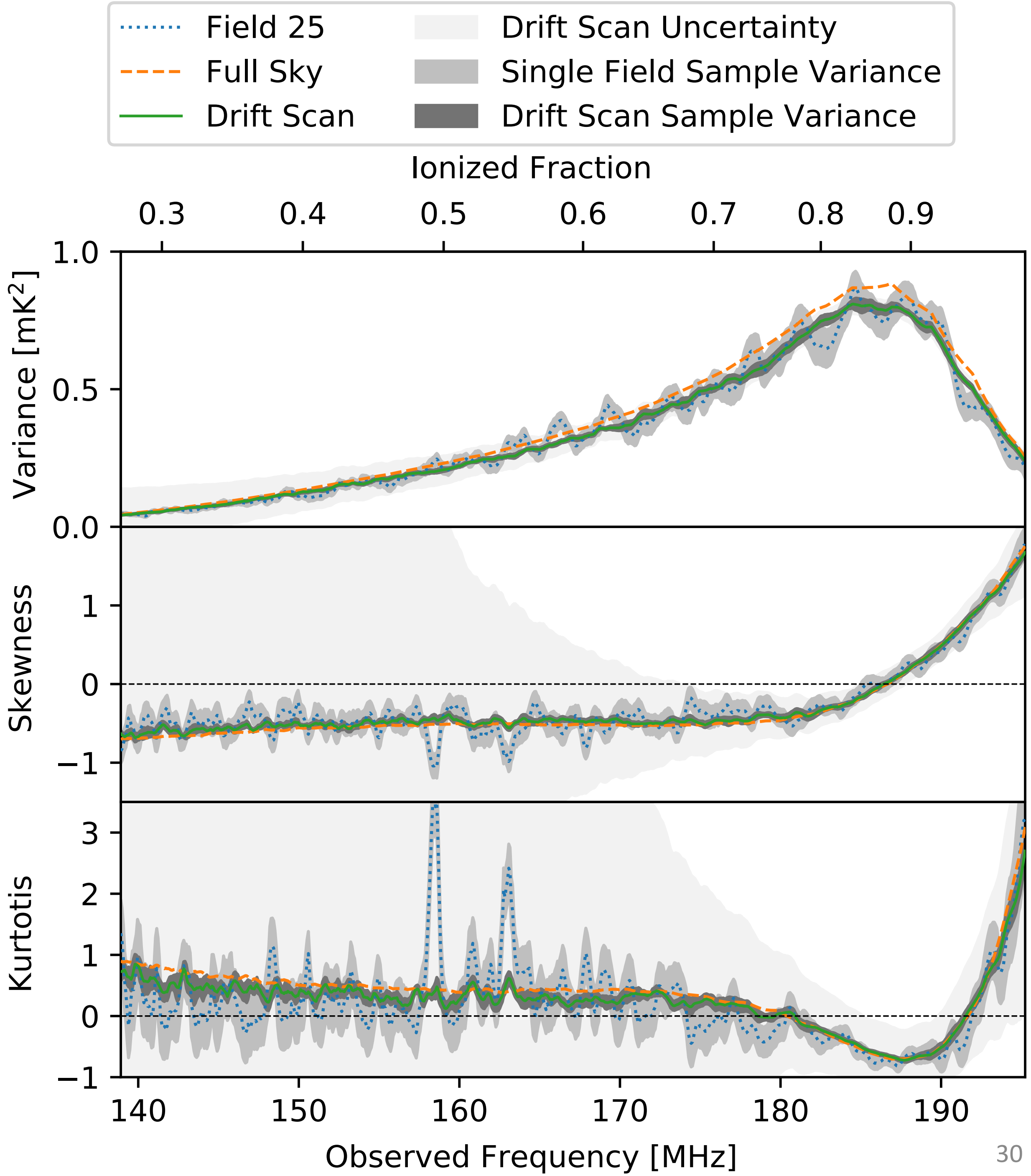

How to Deal with Foreground?

- Subtracting foreground is hard to do
- “Avoiding” foreground is easier to do
- Foreground is contained in a wedge-shape region in the 2D Fourier space
- See, e.g., Morales et al., ApJ, 752, 2, (2012)

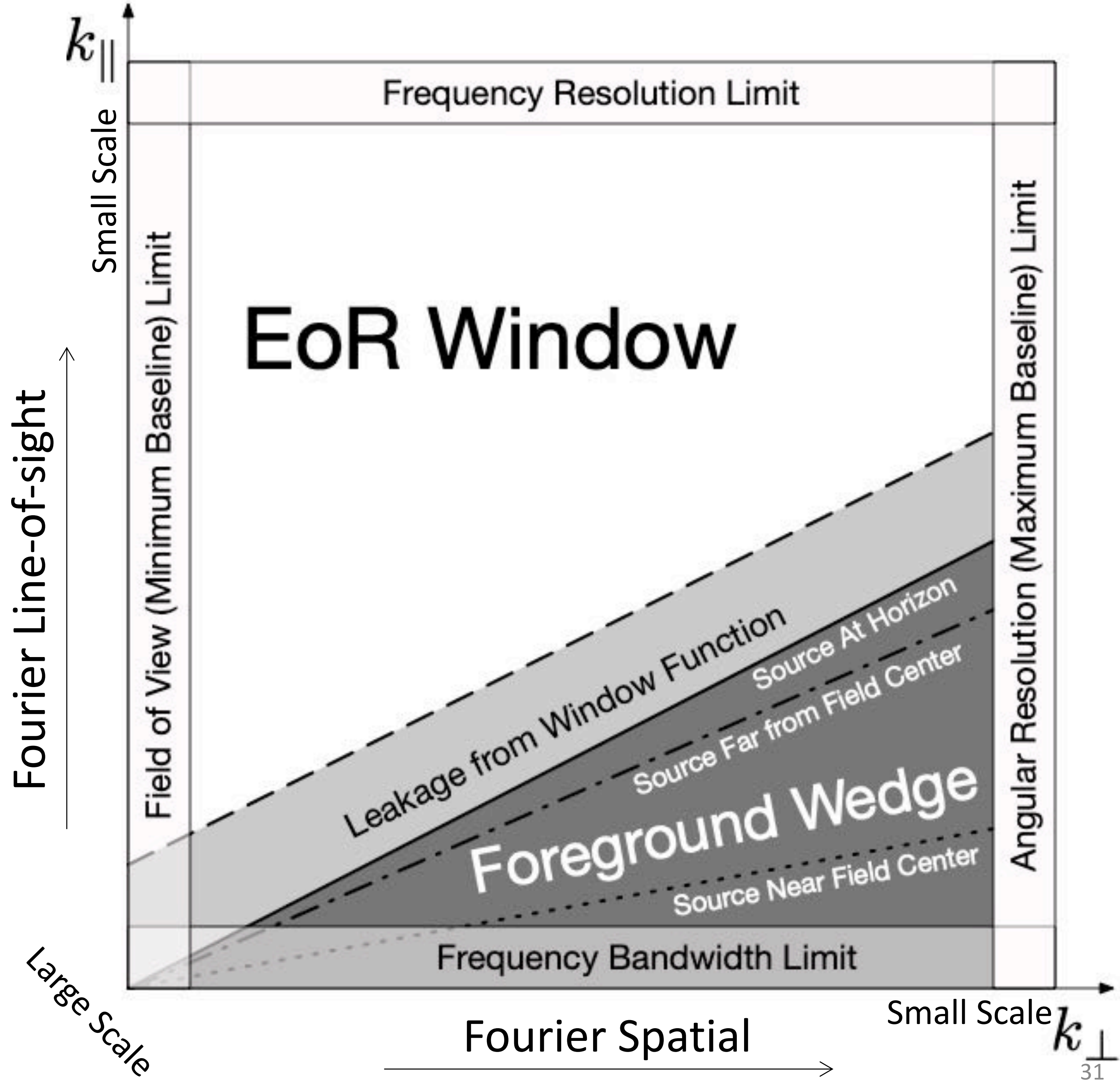

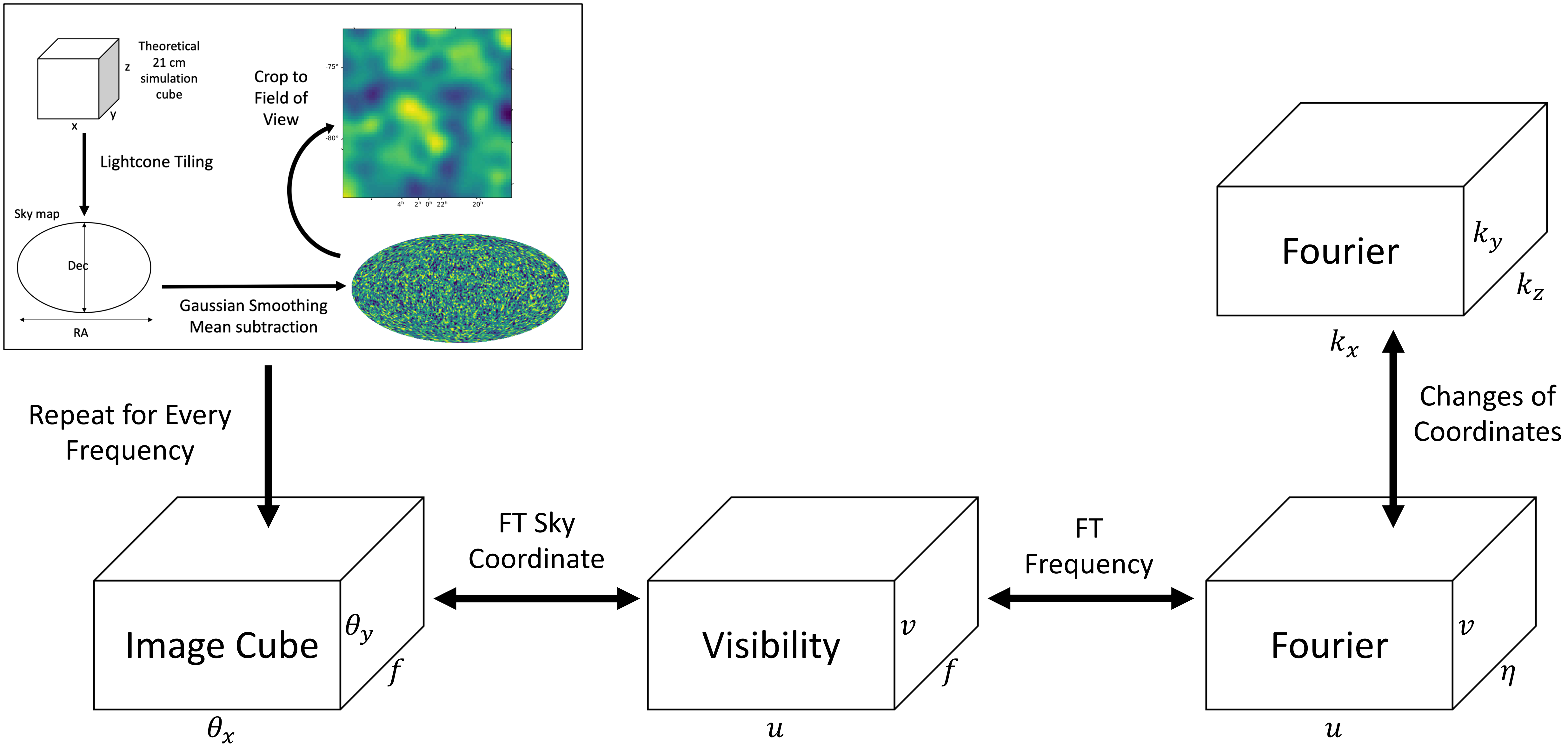
Theoretical 21 cm simulation cube
x
y
z
Lightcone Tiling
Sky map
Dec
RA
Gaussian Smoothing
Mean subtraction
Crop to Field of View
Repeat for Every Frequency
Image Cube
θ_x
θ_y
f
FT Sky Coordinate
Visibility
u
v
f
FT Frequency
Fourier
u
v
η
Changes of Coordinates
Fourier
k_x
k_y
k_z

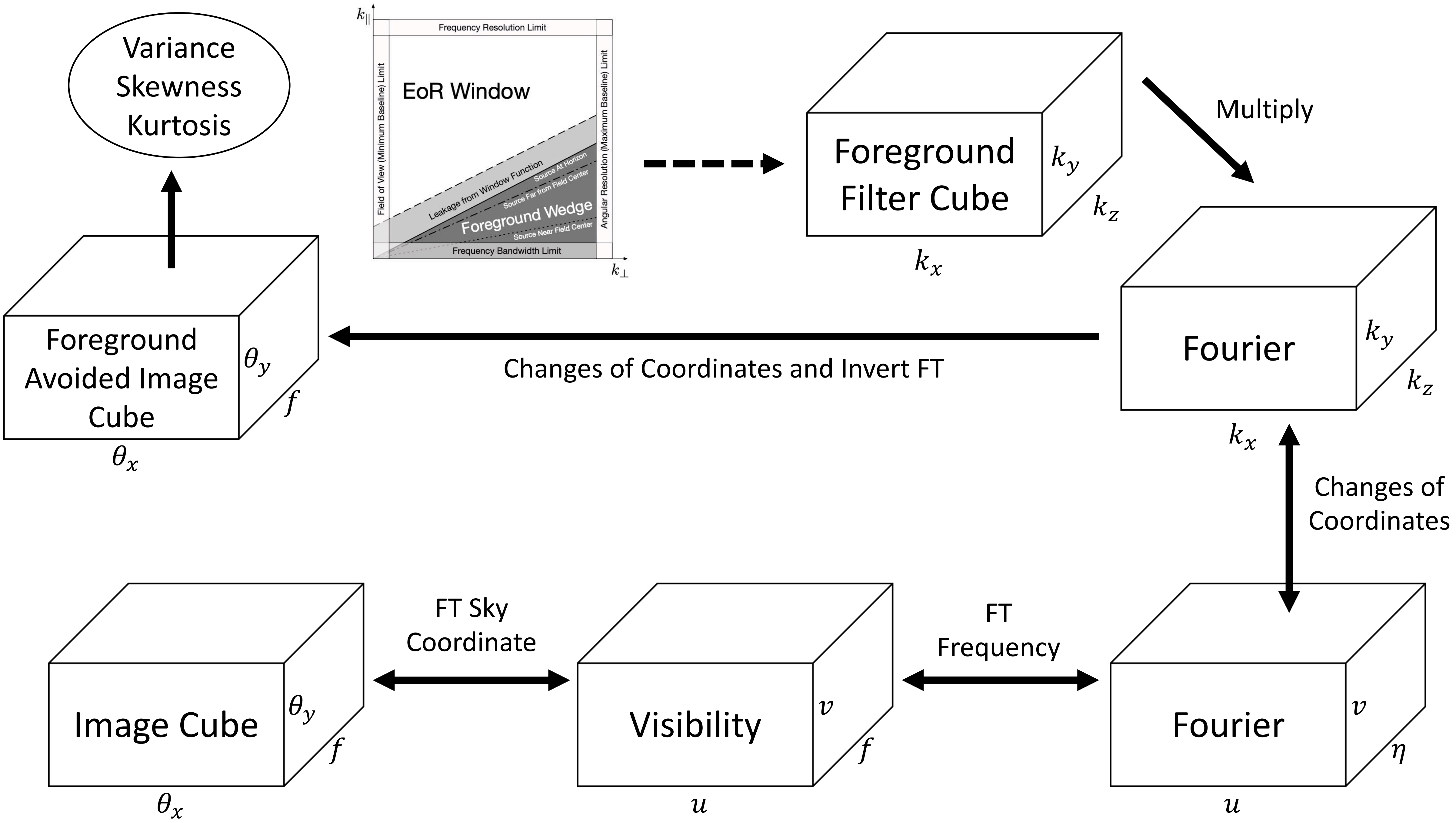
Variance
Skewness
Kurtosis
$k_{\parallel}$
Frequency Resolution Limit
EoR Window
Field of View (Minimum Baseline) Limit
Angular Resolution (Maximum Baseline) Limit
Leakage from Window Function
Source At Horizon
Source Far from Field Center
Foreground Wedge
Source Near Field Center
Frequency Bandwidth Limit
$k_{\perp}$
Foreground Filter Cube
k_y
k_z
k_x
Multiply
Foreground Avoided Image Cube
θ_y
f
θ_x
Changes of Coordinates and Invert FT
Fourier
k_y
k_z
k_x
Changes of Coordinates
Image Cube
θ_y
f
θ_x
FT Sky Coordinate
Visibility
v
f
u
FT Frequency
Fourier
v
η
u

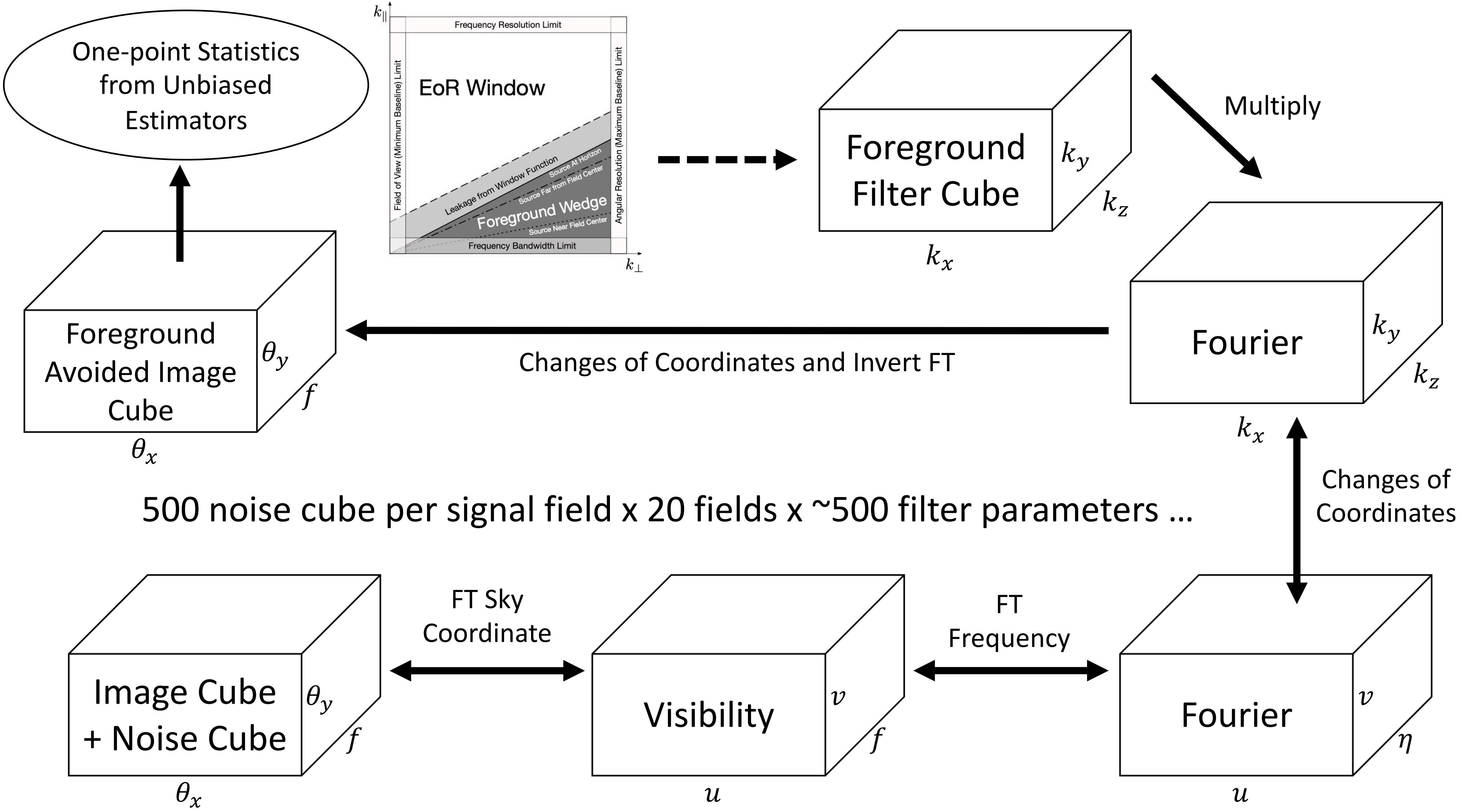
One-point Statistics from Unbiased Estimators
$k_\parallel$
Frequency Resolution Limit
Field of View (Minimum Baseline) Limit
EoR Window
Angular Resolution (Maximum Baseline) Limit
Leakage from Window Function
Source At Horizon
Source Far from Field Center
Foreground Wedge
Source Near Field Center
Frequency Bandwidth Limit
$k_\perp$
Foreground Filter Cube
k_y
k_z
k_x
Multiply
Foreground Avoided Image Cube
θ_y
f
θ_x
Changes of Coordinates and Invert FT
Fourier
k_y
k_z
k_x
Changes of Coordinates
500 noise cube per signal field x 20 fields x ~500 filter parameters …
Image Cube + Noise Cube
θ_y
f
θ_x
FT Sky Coordinate
Visibility
v
f
u
FT Frequency
Fourier
v
η
u

Foreground Avoided Intensity Maps

- 8-MHz Rolling Filter
- HERA350

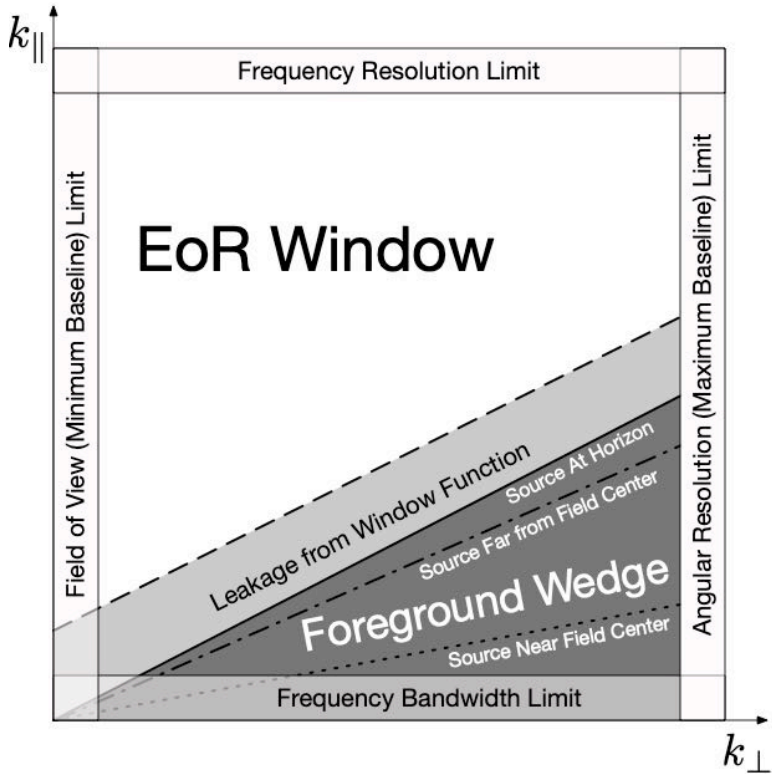

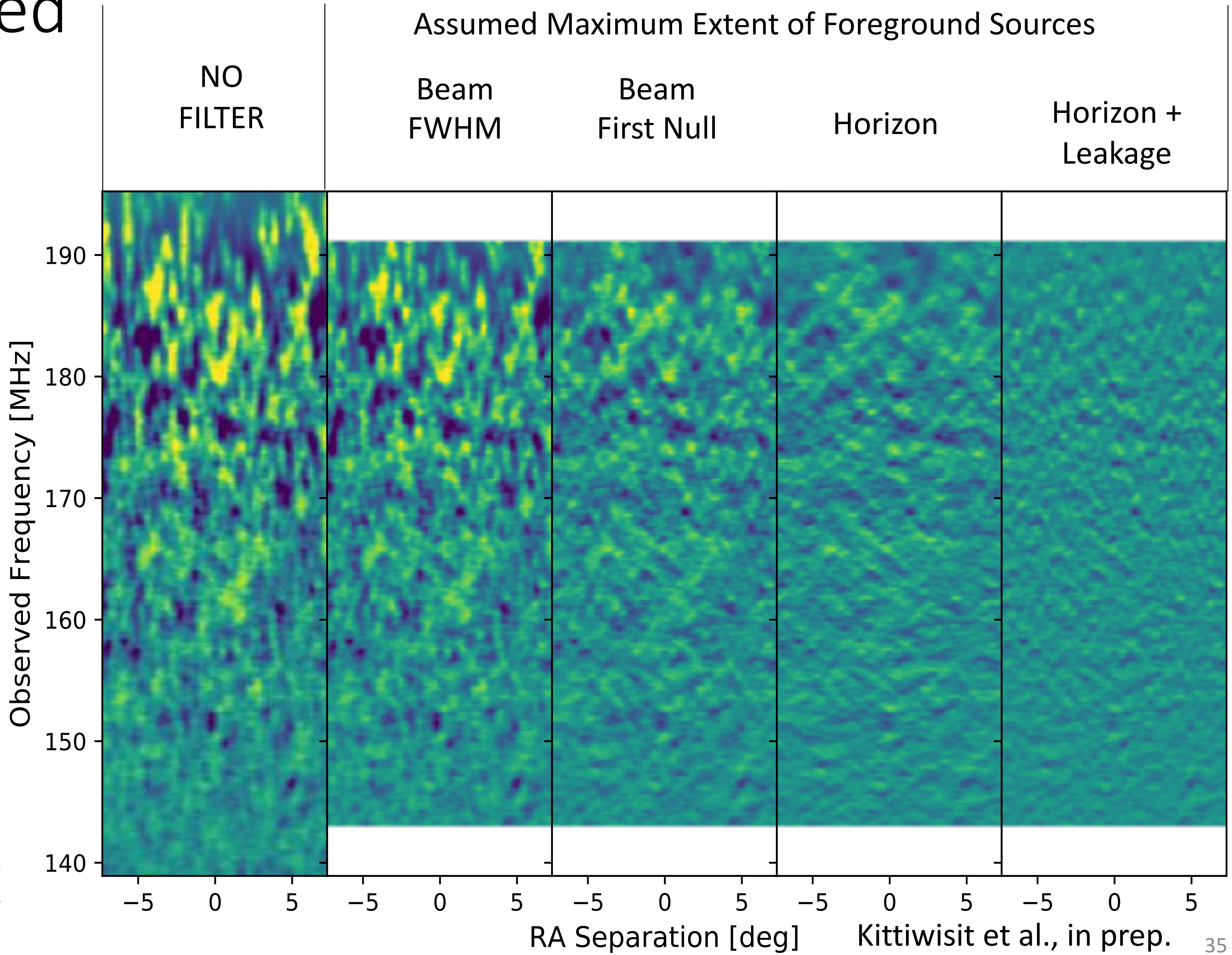

Kittiwisit et al., in prep.

Prediction for HERA - Foreground Avoidance Regime

- 1 MHz channel, 2 year integration
- Need to control leakage from Fourier transform (or integrate much longer)

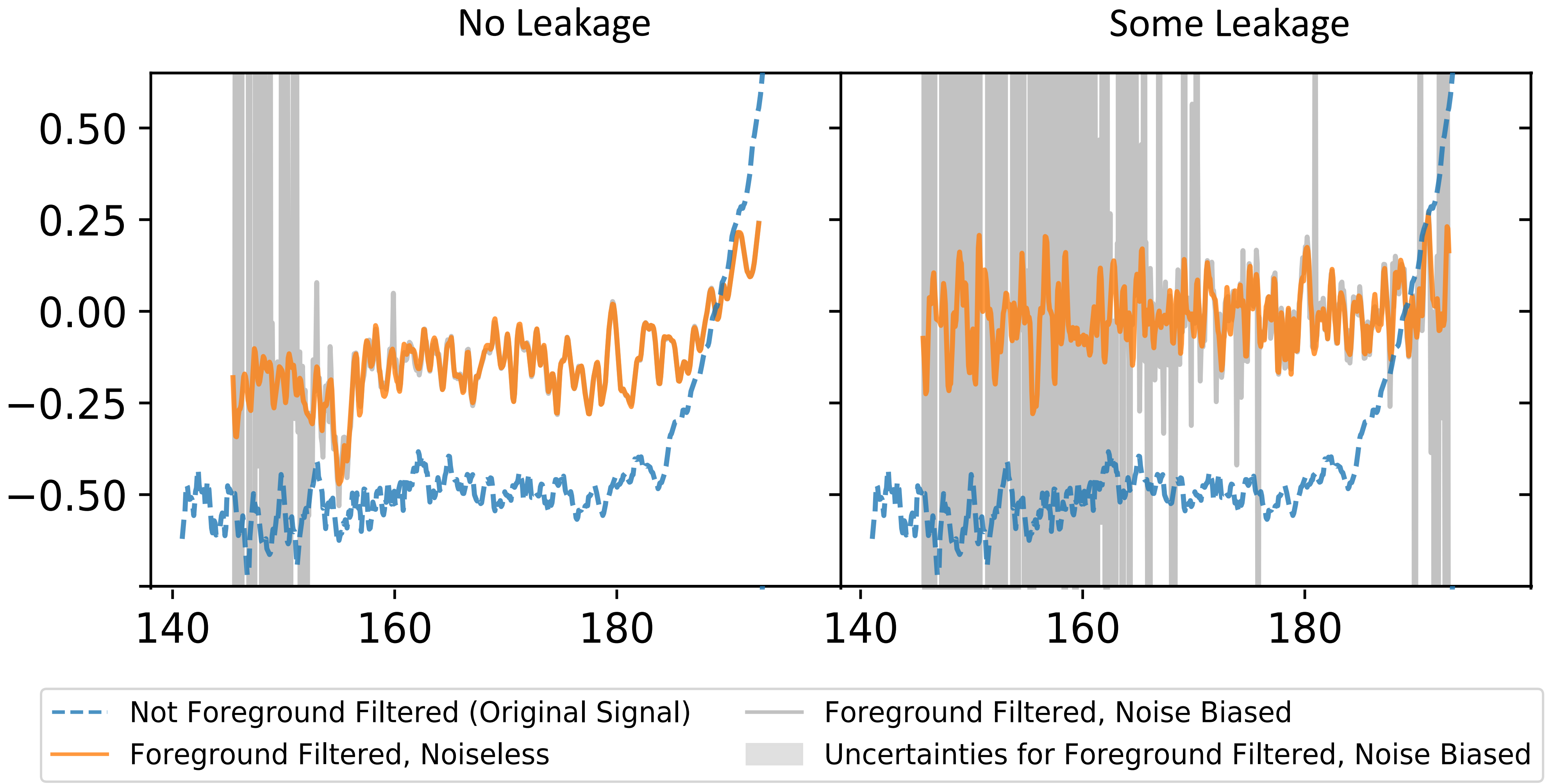

Kittiwisit et al., in prep.

Part II – Summary

- One-point statistics of 21 cm signal
  - Describe the shape of the PDF of 21 cm fluctuations
  - Check for non-Gaussainity in reionization
  - Infer different phases of reionization
  - Distinguish different reionization model (e.g., Watkinson et al. 2014)
- Can HERA measure 21 cm one-point statistics?
  - Yes, if we can mitigate the foreground
  - In the foreground avoidance regime, we need to control spectral leakage
  - We need to explore foreground subtraction regime
  - What kind of reionization physics can we infer?

Ionospheric Study with Low-frequency Radio Array

- Anisotropic plasma density affects incoming foreground wavefronts and must be corrected in EoR analysis.

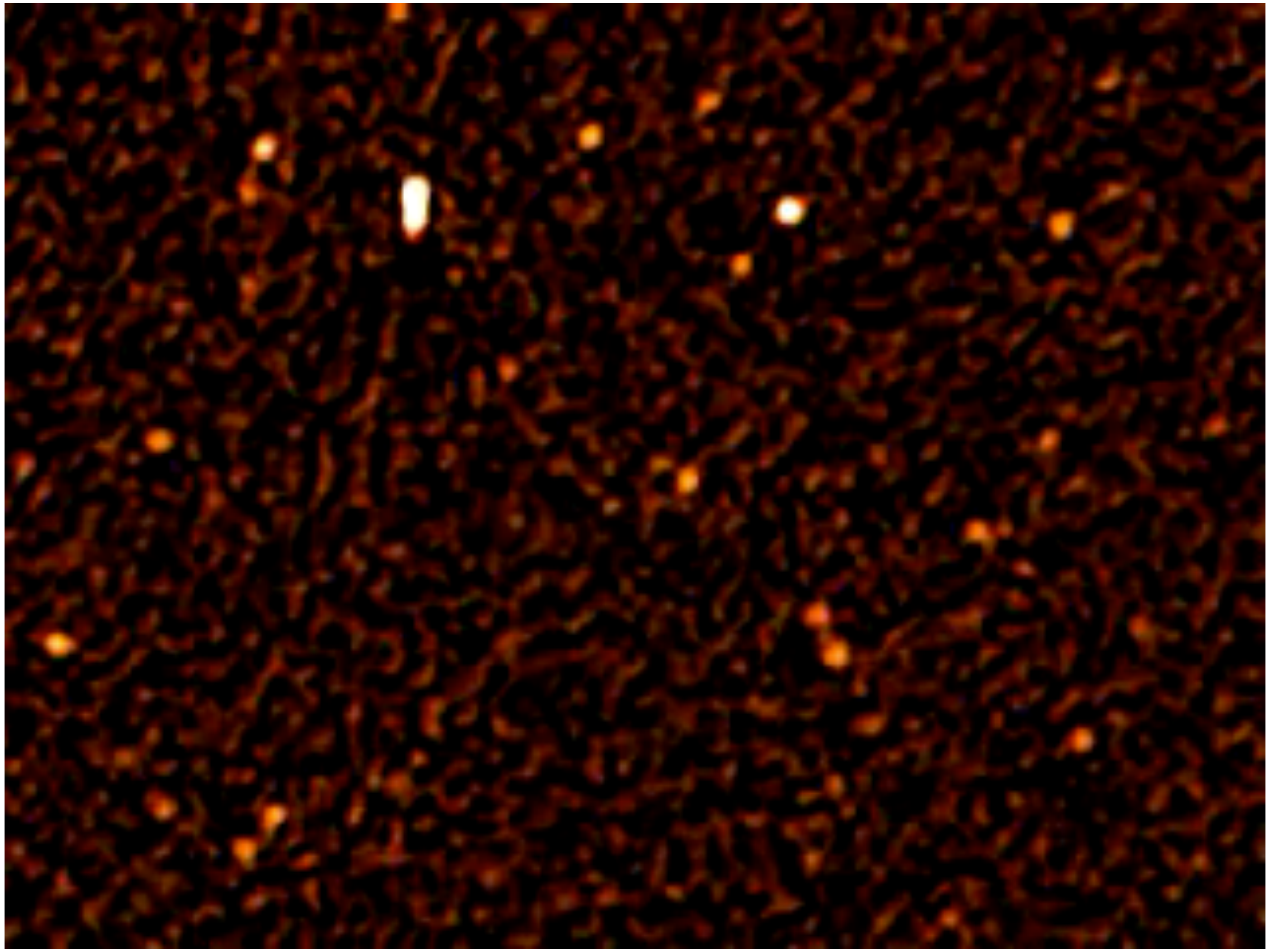

See https://youtu.be/5KWGDx0fq50 for the movie version of the figure

Ionospheric Study with Low-frequency Radio Array

- Anisotropic plasma density affects incoming foreground wavefronts and must be corrected in EoR analysis.
- Loi et al. 2016, Geophysical Research Letters, probed the plasma movements in the MWA data sets.

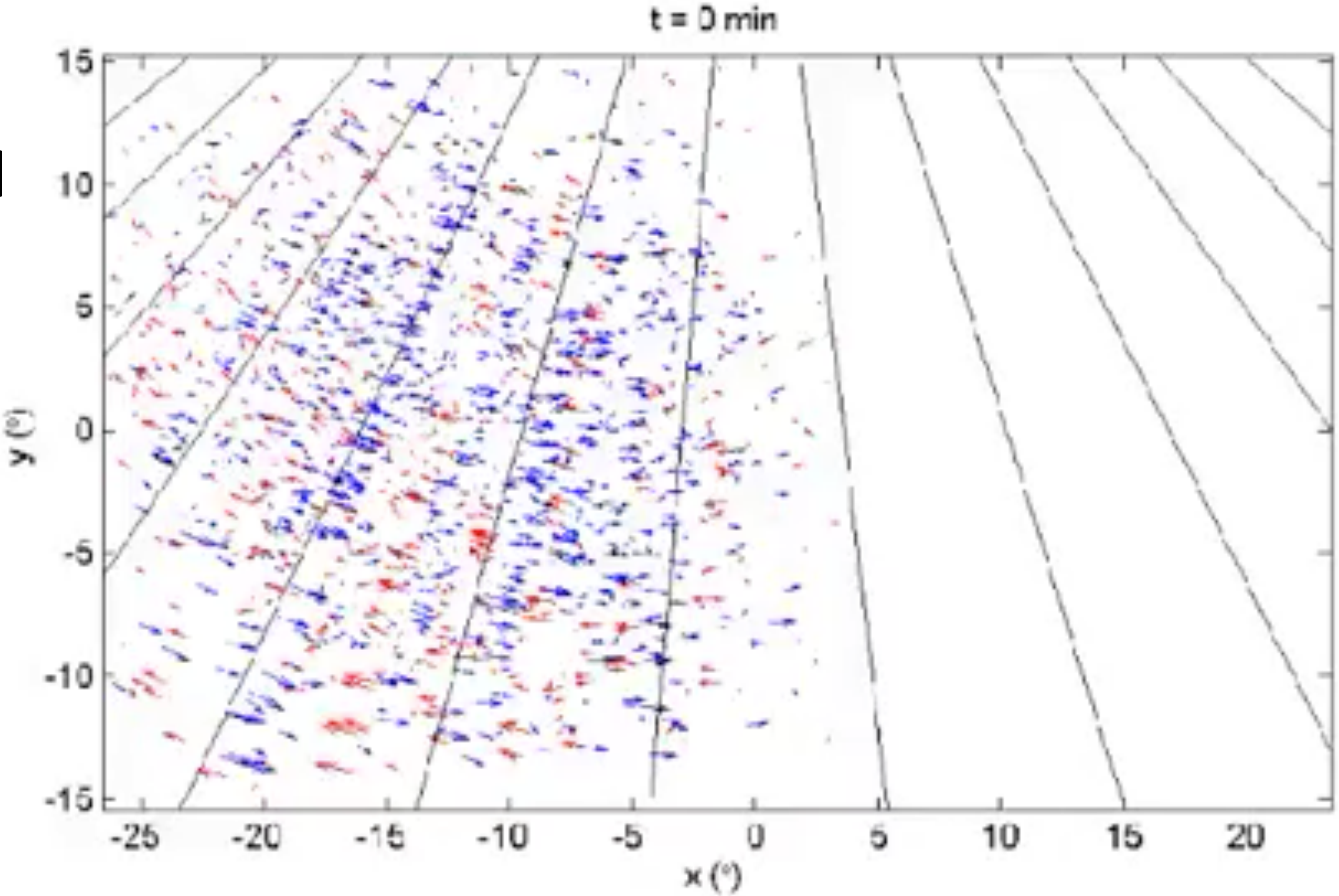

See https://youtu.be/rYXuZsNWGmg for the movie version of the figure

Ionospheric Study with Low-frequency Radio Array

- Anisotropic plasma density affects incoming foreground wavefronts and must be corrected in EoR analysis.
- Loi et al., 2016, Geophysical Research Letters, probed the plasma movements in the MWA data sets and visualized the plasma tubes.
- See Jordan et al., 2017 and Trott et al., 2018 for recent application to EoR analysis.

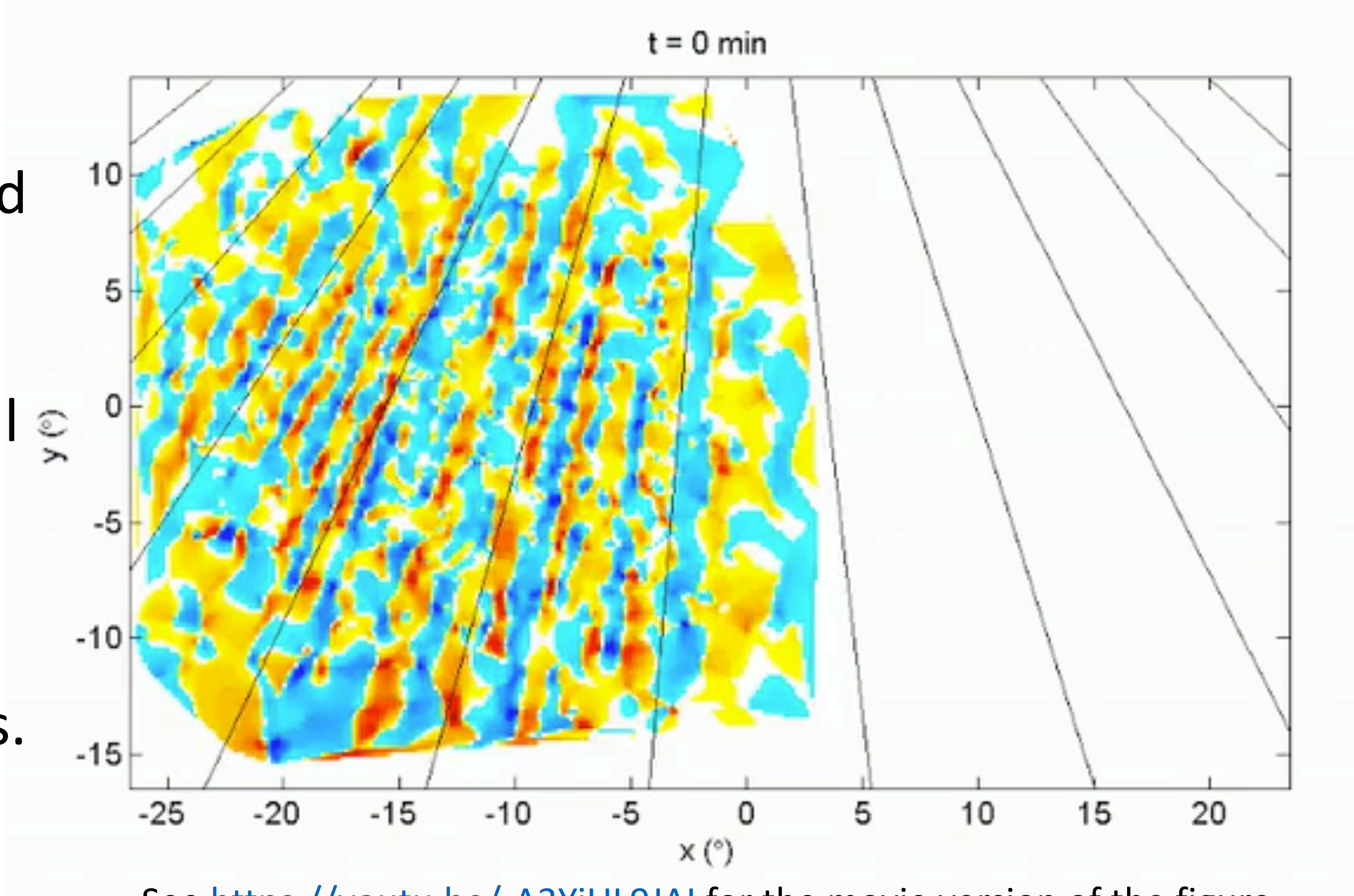

See https://youtu.be/-A3YjUL9JAI for the movie version of the figure

Radio Detection of Cosmic Ray Air Showers

- Deploy scintillator to trigger and confirm radio detection of cosmic-rays
  - LOFAR Radboud Air Shower Array (see Buitink et al. 2017, Nature)
- Or self-triggered
  - Demonstrated by LWA-OWVR
  - GRAND (http://grand.cnrs.fr/)
- See Schroder 2017, Prog.Part.Nucl.Phys., 93, 1-68 for recent review

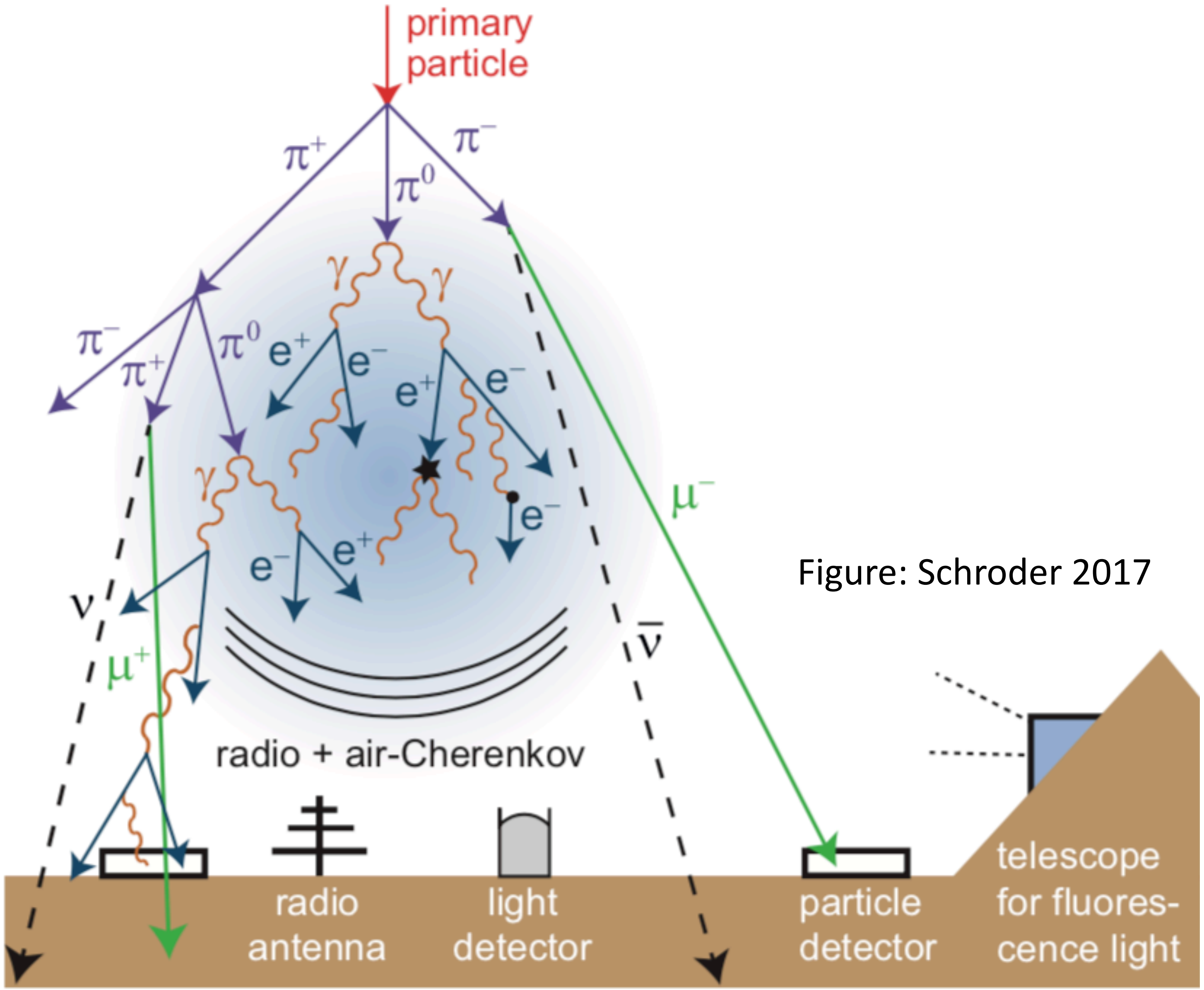

Figure: Schroder 2017

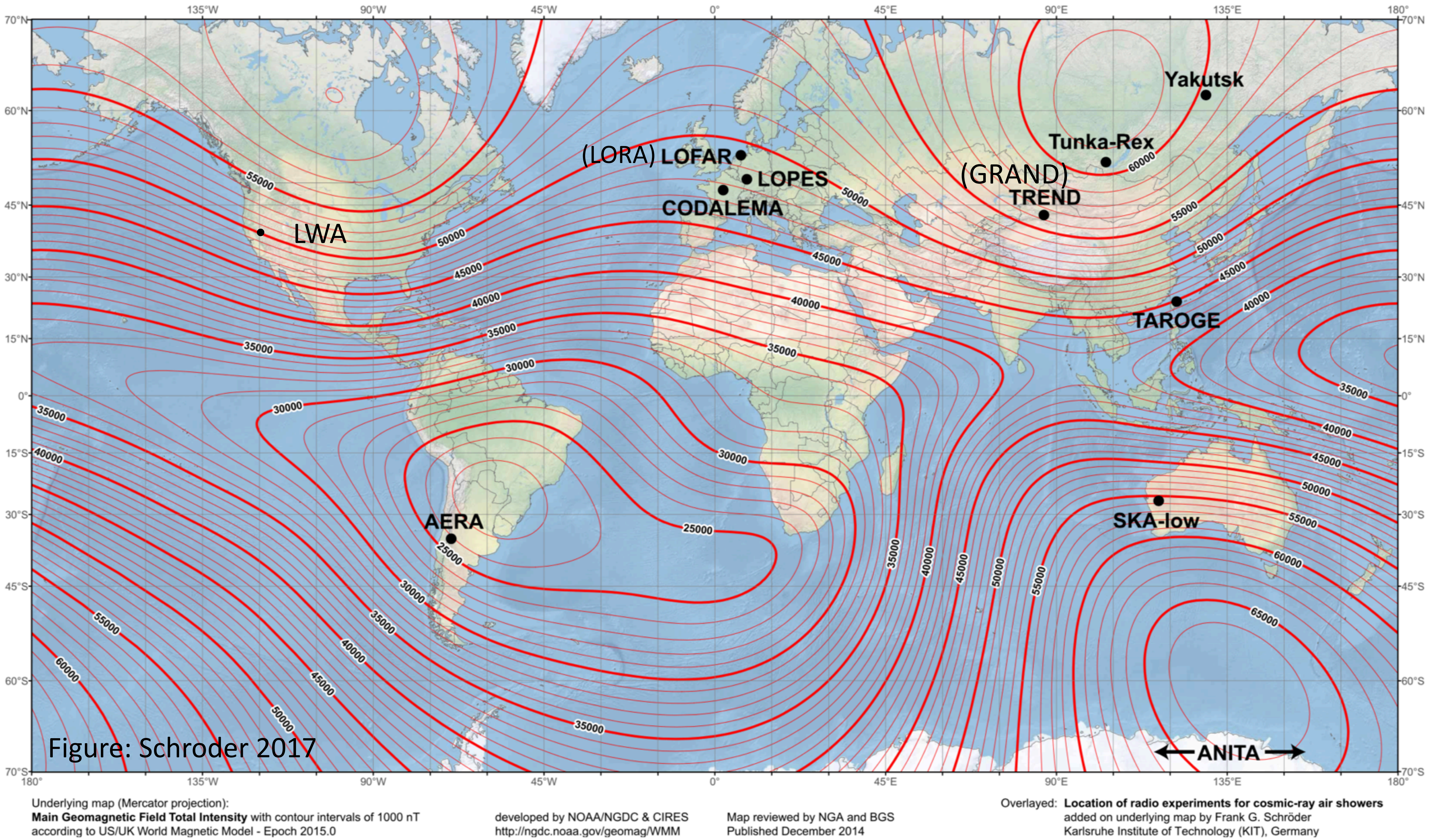

Yakutsk
Tunka-Rex
(GRAND)
TREND
(LORA) LOFAR
LOPES
CODALEMA
LWA
TAROGE
AERA
SKA-low
ANITA
Figure: Schroder 2017
Underlying map (Mercator projection):
Main Geomagnetic Field Total Intensity with contour intervals of 1000 nT
according to US/UK World Magnetic Model - Epoch 2015.0
developed by NOAA/NGDC & CIRES
http://ngdc.noaa.gov/geomag/WMM
Map reviewed by NGA and BGS
Published December 2014
Overlayed: Location of radio experiments for cosmic-ray air showers
added on underlying map by Frank G. Schröder
Karlsruhe Institute of Technology (KIT), Germany

Self-triggered Detection at the Owens Valley Long Wavelength Array

Credit: Monroe's Thesis, Caltech, 2018

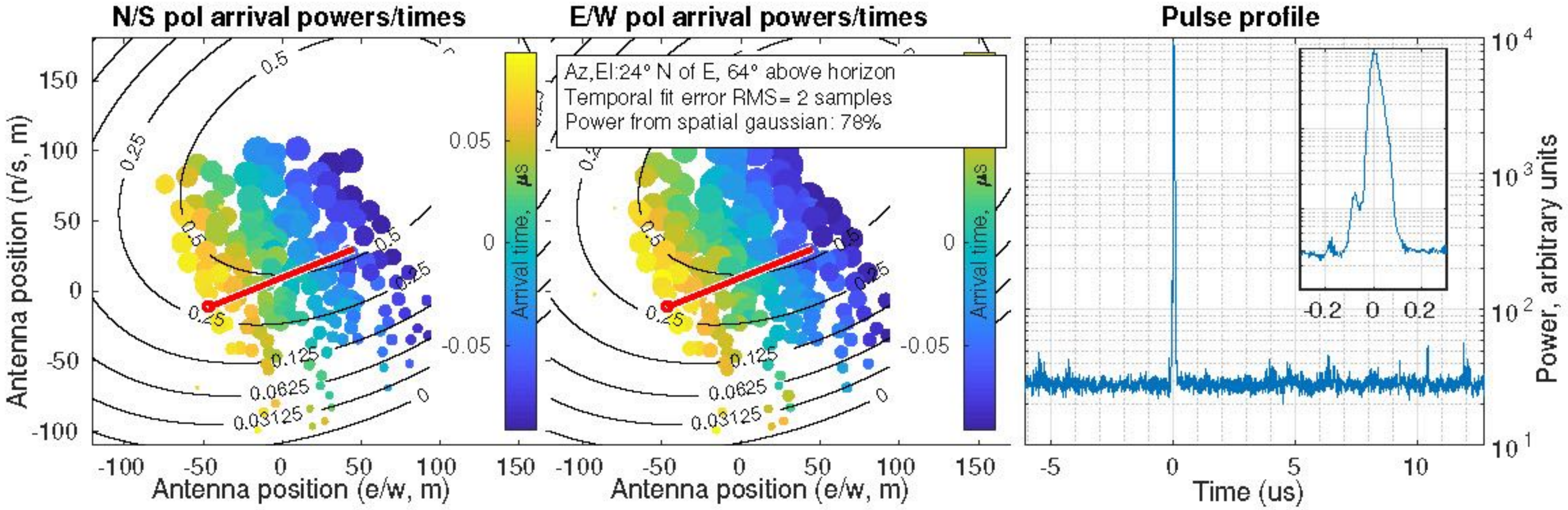

Conclusion

- Low-frequency radio observations are exciting new frontiers for cosmology, astrophysics, ionospheric sciences, particle physics, and beyond
- Challenging due to complication from complex instruments and requirements for data processing
- Reionization and Cosmic Dawn is the main driver, but other science cases are as exciting